The Astrophysical Journal, 821:56 (25pp), 2016 April 10 doi:10.3847/0004-637X/821/1/56

SPACE TELESCOPE AND OPTICAL REVERBERATION MAPPING PROJECT. III. OPTICAL CONTINUUM EMISSION AND BROADBAND TIME DELAYS IN NGC 5548

M. M. Fausnaugh[1], K. D. Denney[1,2,63], A. J. Barth[3], M. C. Bentz[4], M. C. Bottorff[5], M. T. Carini[6], K. V. Croxall[1,2], G. De Rosa[1,2,7], M. R. Goad[8], Keith Horne[9], M. D. Joner[10], S. Kaspi[11,12], M. Kim[13], S. A. Klimanov[14], C. S. Kochanek[1,2], D. C. Leonard[15], H. Netzer[11], B. M. Peterson[1,2], K. Schnülle[16], S. G. Sergeev[17], M. Vestergaard[18,19], W.-K. Zheng[20], Y. Zu[1,21], M. D. Anderson[4], P. Arévalo[22], C. Bazhaw[4], G. A. Borman[17], T. A. Boroson[23], W. N. Brandt[24,25,26], A. A. Breeveld[27], B. J. Brewer[28], E. M. Cackett[29], D. M. Crenshaw[4], E. Dalla Bontà[30,31], A. De Lorenzo-Cáceres[9], M. Dietrich[32,33], R. Edelson[34], N. V. Efimova[14], J. Ely[7], P. A. Evans[8], A. V. Filippenko[20], K. Flatland[15], N. Gehrels[35], S. Geier[36,37,38], J. M. Gelbord[39,40], L. Gonzalez[15], V. Gorjian[41], C. J. Grier[1,24,25], D. Grupe[42], P. B. Hall[43], S. Hicks[6], D. Horenstein[4], T. Hutchison[5], M. Im[44], J. J. Jensen[18], J. Jones[4], J. Kaastra[45,46,47], B. C. Kelly[48], J. A. Kennea[23], S. C. Kim[13], K. T. Korista[49], G. A. Kriss[7,50], J. C. Lee[13], P. Lira[51], F. MacInnis[5], E. R. Manne-Nicholas[4], S. Mathur[1,2], I. M. McHardy[52], C. Montouri[53], R. Musso[5], S. V. Nazarov[17], R. P. Norris[4], J. A. Nousek[24], D. N. Okhmat[17], A. Pancoast[54,64], I. Papadakis[55,56], J. R. Parks[4], L. Pei[3], R. W. Pogge[1,2], J.-U. Pott[16], S. E. Rafter[12,57], H.-W. Rix[16], D. A. Saylor[4], J. S. Schimoia[1,58], M. Siegel[23], M. Spencer[10], D. Starkey[9], H.-I. Sung[13], K. G. Teems[4], T. Treu[48,59,65], C. S. Turner[4], P. Uttley[60], C. Villforth[61], Y. Weiss[12], J.-H. Woo[44], H. Yan[62], and S. Young[34]

[1] Department of Astronomy, The Ohio State University, 140 W 18th Ave., Columbus, OH 43210, USA
[2] Center for Cosmology and AstroParticle Physics, The Ohio State University, 191 West Woodruff Ave., Columbus, OH 43210, USA
[3] Department of Physics and Astronomy, 4129 Frederick Reines Hall, University of California, Irvine, CA 92697, USA
[4] Department of Physics and Astronomy, Georgia State University, 25 Park Place, Suite 605, Atlanta, GA 30303, USA
[5] Fountainwood Observatory, Department of Physics FJS 149, Southwestern University, 1011 E. University Ave., Georgetown, TX 78626, USA
[6] Department of Physics and Astronomy, Western Kentucky University, 1906 College Heights Blvd. #11077, Bowling Green, KY 42101, USA
[7] Space Telescope Science Institute, 3700 San Martin Dr., Baltimore, MD 21218, USA
[8] University of Leicester, Department of Physics and Astronomy, Leicester, LE1 7RH, UK
[9] SUPA Physics and Astronomy, University of St. Andrews, Fife, KY16 9SS Scotland, UK
[10] Department of Physics and Astronomy, N283 ESC, Brigham Young University, Provo, UT 84602-4360, USA
[11] School of Physics and Astronomy, Raymond and Beverly Sackler Faculty of Exact Sciences, Tel Aviv University, Tel Aviv 69978, Israel
[12] Physics Department, Technion, Haifa 32000, Israel
[13] Korea Astronomy and Space Science Institute, Korea
[14] Pulkovo Observatory, 196140 St. Petersburg, Russia
[15] Department of Astronomy, San Diego State University, San Diego, CA 92182-1221, USA
[16] Max Planck Institut für Astronomie, Königstuhl 17, D-69117 Heidelberg, Germany
[17] Crimean Astrophysical Observatory, P/O Nauchny, Crimea 298409, Russia
[18] Dark Cosmology Centre, Niels Bohr Institute, University of Copenhagen, Juliane Maries Vej 30, DK-2100 Copenhagen, Denmark
[19] Steward Observatory, University of Arizona, 933 North Cherry Ave., Tucson, AZ 85721, USA
[20] Department of Astronomy, University of California, Berkeley, CA 94720-3411, USA
[21] Department of Physics, Carnegie Mellon University, 5000 Forbes Ave., Pittsburgh, PA 15213, USA
[22] Instituto de Física y Astronomía, Facultad de Ciencias, Universidad de Valparaíso, Gran Bretana N 1111, Playa Ancha, Valparaíso, Chile
[23] Las Cumbres Global Telescope Network, 6740 Cortona Dr., Suite 102, Santa Barbara, CA 93117, USA
[24] Department of Astronomy and Astrophysics, Eberly College of Science, The Pennsylvania State University, 525 Davey Laboratory, University Park, PA 16802, USA
[25] Institute for Gravitation and the Cosmos, The Pennsylvania State University, University Park, PA 16802, USA
[26] Department of Physics, The Pennsylvania State University, 104 Davey Lab, University Park, PA 16802, USA
[27] Mullard Space Science Laboratory, University College London, Holmbury St. Mary, Dorking, Surrey RH5 6NT, UK
[28] Department of Statistics, The University of Auckland, Private Bag 92019, Auckland 1142, New Zealand
[29] Department of Physics and Astronomy, Wayne State University, 666 W. Hancock St., Detroit, MI 48201, USA
[30] Dipartimento di Fisica e Astronomia "G. Galilei," Università di Padova, Vicolo dell'Osservatorio 3, I-35122 Padova, Italy
[31] INAF-Osservatorio Astronomico di Padova, Vicolo dell'Osservatorio 5 I-35122, Padova, Italy
[32] Department of Physics and Astronomy, Ohio University, Athens, OH 45701, USA
[33] Department of Earth, Environment, and Physics, Worcester State University, 486 Chandler St., Worcester, MA 01602, USA
[34] Department of Astronomy, University of Maryland, College Park, MD 20742-2421, USA
[35] Astrophysics Science Division, NASA Goddard Space Flight Center, Greenbelt, MD 20771, USA
[36] Instituto de Astrofísica de Canarias, E-38200 La Laguna, Tenerife, Spain
[37] Departamento de Astrofísica, Universidad de La Laguna, E-38206 La Laguna, Tenerife, Spain
[38] Gran Telescopio Canarias (GRANTECAN), E-38205 San Cristóbal de La Laguna, Tenerife, Spain
[39] Spectral Sciences Inc., 4 Fourth Ave., Burlington, MA 01803, USA
[40] Eureka Scientific Inc., 2452 Delmer St., Suite 100, Oakland, CA 94602, USA
[41] MS 169-327, Jet Propulsion Laboratory, California Institute of Technology, 4800 Oak Grove Dr., Pasadena, CA 91109, USA
[42] Space Science Center, Morehead State University, 235 Martindale Dr., Morehead, KY 40351, USA
[43] Department of Physics and Astronomy, York University, Toronto, ON M3J 1P3, Canada
[44] Astronomy Program, Department of Physics & Astronomy, Seoul National University, Seoul, Korea
[45] SRON Netherlands Institute for Space Research, Sorbonnelaan 2, 3584 CA Utrecht, The Netherlands
[46] Department of Physics and Astronomy, Univeristeit Utrecht, P.O. Box 80000, 3508 Utrecht, The Netherlands
[47] Leiden Observatory, Leiden University, P.O. Box 9513, 2300 RA Leiden, The Netherlands
[48] Department of Physics, University of California, Santa Barbara, CA 93106, USA
[49] Department of Physics, Western Michigan University, 1120 Everett Tower, Kalamazoo, MI 49008-5252, USA
[50] Department of Physics and Astronomy, Johns Hopkins University, Baltimore, MD 21218, USA
[51] Departamento de Astronomia, Universidad de Chile, Camino del Observatorio 1515, Santiago, Chile
[52] University of Southampton, Highfield, Southampton, SO17 1BJ, UK

[53] DiSAT, Universita dell'Insubria, via Valleggio 11, I-22100, Como, Italy
[54] Harvard-Smithsonian Center for Astrophysics, 60 Garden St., Cambridge, MA 02138, USA
[55] Department of Physics and Institute of Theoretical and Computational Physics, University of Crete, GR-71003 Heraklion, Greece
[56] IESL, Foundation for Research and Technology, GR-71110 Heraklion, Greece
[57] Department of Physics, Faculty of Natural Sciences, University of Haifa, Haifa 31905, Israel
[58] Instituto de Física, Universidade Federal do Rio do Sul, Campus do Vale, Porto Alegre, Brazil
[59] Department of Physics and Astronomy, University of California, Los Angeles, CA 90095-1547, USA
[60] Astronomical Institute "Anton Pannekoek,"University of Amsterdam, Postbus 94249, NL-1090 GE Amsterdam, The Netherlands
[61] University of Bath, Department of Physics, Claverton Down, BA2 7AY, Bath, UK
[62] Department of Physics and Astronomy, University of Missouri, Columbia, MO 65211, USA
Received 2015 October 19; accepted 2016 February 25; published 2016 April 11

ABSTRACT

We present ground-based optical photometric monitoring data for NGC 5548, part of an extended multiwavelength reverberation mapping campaign. The light curves have nearly daily cadence from 2014 January to July in nine filters (*BVRI* and *ugriz*). Combined with ultraviolet data from the *Hubble Space Telescope* and *Swift*, we confirm significant time delays between the continuum bands as a function of wavelength, extending the wavelength coverage from 1158 Å to the *z* band (~9160 Å). We find that the lags at wavelengths longer than the *V* band are equal to or greater than the lags of high-ionization-state emission lines (such as He II λ1640 and λ4686), suggesting that the continuum-emitting source is of a physical size comparable to the inner broad-line region (BLR). The trend of lag with wavelength is broadly consistent with the prediction for continuum reprocessing by an accretion disk with $\tau \propto \lambda^{4/3}$. However, the lags also imply a disk radius that is 3 times larger than the prediction from standard thin-disk theory, assuming that the bolometric luminosity is 10% of the Eddington luminosity ($L = 0.1L_{\rm Edd}$). Using optical spectra from the Large Binocular Telescope, we estimate the bias of the interband continuum lags due to BLR emission observed in the filters. We find that the bias for filters with high levels of BLR contamination (~20%) can be important for the shortest continuum lags and likely has a significant impact on the *u* and *U* bands owing to Balmer continuum emission.

Key words: galaxies: active – galaxies: individual (NGC 5548) – galaxies: nuclei – galaxies: Seyfert

Supporting material: machine-readable tables

1. INTRODUCTION

The continuum emission of radio-quiet active galactic nuclei (AGNs) is believed to originate in an accretion disk around a supermassive black hole (SMBH). At accretion rates and masses appropriate for SMBHs, geometrically thin, optically thick accretion disks have maximum temperatures of $\sim 10^5$–10^6 K, naturally accounting for the characteristic peak of AGN spectral energy distributions (SEDs) in the far-UV (Burbidge 1967; Shakura & Sunyaev 1973; Shields 1978). However, a large variety of competing models of the accretion flow exist, such as thick-disk geometries at extremely super- or sub-Eddington accretion rates (Abramowicz et al. 1988; Narayan & Yi 1995). In addition, AGNs exhibit nonthermal X-ray emission, which requires a hot plasma component or "corona" (e.g., Haardt & Maraschi 1991; Chakrabarti & Titarchuk 1995). The potential configurations and complex interplay between the hot corona and accretion disk admit a wide range of models with many free parameters, and searching for the unique observational signatures of a given disk model is very challenging (Sun & Malkan 1989; Laor et al. 1997; Koratkar & Blaes 1999; Vestergaard & Wilkes 2001; Telfer et al. 2002; Kishimoto et al. 2004, and references therein).

Reverberation mapping (RM; Blandford & McKee 1982; Peterson 1993, 2014) can provide insight into the structure of the accretion disk and has become a standard tool for AGN astrophysics over the past 25 yr (Clavel et al. 1991; Horne et al. 1991; Peterson et al. 1991, 2004; Kaspi et al. 2000; Bentz et al. 2009; Denney et al. 2010; Grier et al. 2013b; Pancoast et al. 2014; Pei et al. 2014; Barth et al. 2015, and references therein). The basic principle of RM is that emission at two different wavelengths is causally connected, so that the time delay (or lag) between two light curves represents the light-crossing time within the system and thereby provides a straightforward measurement of the system's physical size. For example, because the AGN continuum powers the prominent emission lines observed in Seyfert galaxy/quasar spectra, the time delays between continuum and broad-line light curves are commonly used to determine the physical extent of the line-emitting gas (the so-called broad-line region [BLR]).

In a similar way, RM techniques can be used to constrain the physical processes governing AGN continuum emission. X-ray emission from the corona may irradiate and heat the accretion disk. If the corona is relatively compact and centrally located, the UV and optical emission would be expected to respond to the incident X-ray flux, "echoing" the X-ray light curve after a time delay corresponding to the light-travel time across the disk (Krolik et al. 1991). On the other hand, X-ray light curves would be expected to lag behind UV and optical light curves if the X-rays are produced by Comptonization of thermal UV/optical disk photons (Haardt & Maraschi 1991). Observational investigations of the relation between X-ray and UV/optical emission have produced ambiguous results. X-rays have been found to lead the optical emission by one to several days in some objects (e.g., Arévalo et al. 2009; Breedt et al. 2010; Shappee et al. 2014; Troyer et al. 2016), but the X-ray variability on long (>1 yr) timescales cannot always account for the optical variations (Uttley et al. 2003; Breedt et al. 2009). In addition, other studies find no long-term X-ray/optical correlations (Maoz et al. 2002), or find optical variations that

[63] NSF Postdoctoral Research Fellow.
[64] Einstein Fellow.
[65] Packard Fellow.

lead the X-rays on shorter timescales (~15 days; Marshall et al. 2008).

RM can also reveal information about the size and structure of the continuum-emitting source. Emission from different portions of the disk peaks at different wavelengths depending on the local disk temperature. By translating the wavelength of the continuum emission into a characteristic temperature, time delays between continuum light curves can be used to map the temperature profile of the disk. The first statistically significant interband time delays were found in NGC 7469 by Wanders et al. (1997) and Collier et al. (1998). Sergeev et al. (2005) carried out intensive optical monitoring of 14 AGNs and found evidence that longer wavelengths lag shorter-wavelength emission. More recent continuum RM campaigns have used the *Swift* observatory (Gehrels et al. 2004) to obtain unprecedentedly well sampled light curves across X-ray, near-UV, and optical wavelengths: Shappee et al. (2014) observed NGC 2617 with *Swift* on a nearly daily basis for several months in 2014, while McHardy et al. (2014) monitored NGC 5548 with ~2-day cadence for approximately 2 yr (excepting seasonal gaps). These studies found trends of lag with wavelength that are well fit by the expectation for X-ray/far-UV reprocessing.

The present study is the third in a series describing the results of the AGN Space Telescope and Optical Reverberation Mapping (STORM) project, an intensive, multiwavelength monitoring campaign of NGC 5548. The AGN STORM campaign is anchored by daily far-UV observations using the Cosmic Origins Spectrograph (COS; Green et al. 2012) on the *Hubble Space Telescope* (*HST*). De Rosa et al. (2015, hereafter Paper I) give a complete introduction to the project and an analysis of the *HST* data. The COS program was complemented by a 4-month broadband photometric monitoring campaign using *Swift*, the first results of which are presented by Edelson et al. (2015, hereafter Paper II). The *Swift* campaign achieved ~0.5-day cadence and detected significant lags between the UV and optical continua, which follow the expected lag–wavelength relation of a thin accretion disk ($\tau \propto \lambda^{4/3}$).

Supplementing these space-based observations are ground-based optical monitoring programs. The present study details the optical broadband photometric monitoring component, which extends the analysis in Paper II using data in nine optical filters with $\lesssim$1-day cadence for 7 months. The similarly intensive ground-based spectroscopic monitoring will be presented by L. Pei et al. (2016, in preparation, hereafter Paper V). In terms of cadence, temporal baseline, and wavelength coverage, the combination of UV and optical observations of the AGN STORM project represents the most complete RM experiment ever conducted.

The present work has three primary goals. The first is to directly compare the far-UV and optical light curves of NGC 5548 over a concurrent monitoring period. The far-UV light curve (~1350 Å) is expected to closely trace the true ionizing continuum ($\leqslant$912 Å), while the optical continuum (~5100 Å) appears to be delayed and somewhat smoothed compared to the UV emission. Since ground-based RM campaigns use the optical continuum as a proxy for the driving continuum light curve, understanding how the continuum emission changes as a function of wavelength is important for understanding any systematic effects in optical RM experiments. The second goal is to search for time delays between the UV and optical data, in an attempt to probe the structure of the continuum-emitting region. However, because broadband filters pick up spectral features that arise in the BLR (e.g., strong emission lines), and these features have large lags relative to the underlying continuum (several days for a Seyfert galaxy such as NGC 5548), interband lags estimated from broadband photometry may be biased indicators of the accretion-disk size. Therefore, our final goal is to estimate the impact of BLR emission on the observed interband time delays.

In Section 2, we describe the observations, data reduction, flux calibration, and general properties of the ground-based photometric light curves. In Section 3, we describe our time-series analysis, measuring the lag as a function of wavelength of the broadband filters. We then explore the impact of BLR emission on the observed interband lags in Section 4. Finally, we discuss our results in Section 5, and we summarize our conclusions in Section 6. Where relevant, we assume a standard cosmological model with $\Omega_m = 0.28$, $\Omega_\Lambda = 0.72$, and $H_0 = 70$ km s^{-1} (Komatsu et al. 2011).

2. OBSERVATIONS AND DATA REDUCTION

In conjunction with the *HST COS* UV RM campaign described in Paper I, NGC 5548 was observed between 2013 December and 2014 August by 16 ground-based observatories in optical broadband filters: Johnson/Cousins *BVRI* and Sloan Digital Sky Survey (SDSS) *ugriz*. A short description of each telescope, the relevant imager, and the number of contributed epochs is given in Table 1. All observatories followed a common reduction protocol: images were first overscan-corrected, bias-subtracted, and flat-fielded following standard procedures. The reduced data, as well as nightly calibration frames, raw images, and observing logs, were then uploaded to a central repository, and the image quality was assessed by eye. Images taken in reasonable atmospheric conditions and free of obvious reduction errors were analyzed as described below.

2.1. Differential Photometry

The analysis is based on the `ISIS` image-subtraction software package (Alard & Lupton 1998). Images are first registered to a common coordinate system, and the images with the lowest backgrounds and best seeing are combined into a high signal-to-noise ratio (S/N) "reference" image. The other images are then rescaled to match the effective exposure time of the reference image. Next, the reference image is convolved with a spatially variable kernel to match the point-spread function (PSF) of each individual epoch and then subtracted to leave the variable flux in each pixel. We use `ISIS`'s built-in photometry package to extract light curves from the subtracted images at the position of the AGN in NGC 5548, in units of differential counts relative to the reference image. Because each telescope/filter/detector combination has slightly different properties (pixel scales, fields of view, gains, etc.), we built reference frames and subtracted images for each unique data set. This procedure corrects for variable seeing conditions and removes nonvariable sources such as host-galaxy starlight, allowing a clean measurement of the variable AGN flux.

2.2. Measurement Uncertainties

The formal errors found by `ISIS` sometimes underestimate the full uncertainties because they only account for local Poisson error contributions. In order to estimate more reliable measurement uncertainties, we examined the residual fluxes of

Table 1
Contributing Observatories

Observatory Name	Obs ID	Aperture	Detector	Pixel Scale	Field of View	Observing Period	Filters	Epochs
Bohyunsan Optical Astronomy Observatory	BOAO	1.8 m	e2v CCD231-84	0.″21	15′ × 15′	Mar–Apr	*V*	5
Crimean Astrophysical Observatory	CrAO	0.7 m	AP7p CCD	1.″76	15′ × 15′	Dec–Jun	*BVRI*	76
Fountainwood Observatory	FWO	0.4 m	SBIG 8300 M	0.″35	19′ × 15′	Jan–Aug	*V*	60
Hard Labor Creek Observatory	HLCO	0.5 m	Apogee USB/Net	0.″75	25′ × 25′	Apr–Jun	*V*	27
La Silla Observatory	GROND	2.2 m	Gamma-ray Burst Optical/ Near-IR Detector	0.″33	5′ × 5′	Feb–Jul	*griz*	6
Las Cumbres Observatory Global Telescope Network	LCOGT	1.0 m	SBIGSTX-16803/ Sinistro CCD-486BI	0.″23 0.″39	16′ × 16′ 27′ × 27′	Jan–Aug	*BV ugriz*	263
Lick Observatory Katzman Automatic Imaging Telescope	KAIT	0.8 m	AP7 CCD	0.″80	7′ × 7′	Jan–Jul	*V*	80
Liverpool Telescope	LT	2.0 m	e2v CCD 231	0.″15	10′ × 10′	Feb–Aug	*ugriz*	120
Maidanak Observatory	MO15	1.5 m	SNUCAM	0.″27	18′ × 18′	Apr–Aug	*BVR*	45
Mt. Laguna Observatory	MLO	1.0 m	CCD2005	0.″41	14′ × 14′	Jun–Aug	*V*	10
Mt. Lemmon Optical Astronomy Observatory	LOAO	1.0 m	KAF-4301E	0.″68	22′ × 22′	Feb–Jul	*V*	26
Nordic Optical Telescope	NOT	2.5 m	e2V CCD42-40	0.″19	6′ × 6′	Apr	*V*	3
Robotically Controlled Telescope	RCT	1.3 m	SITe CCD	0.″30	10′ × 10′	Dec–May	*BV*	55
Svetloe Observatory	SvO	0.4 m	ST-7XME CCD	2.″00	12′ × 8′	Jan–May	*BVRI*	49
West Mountain Observatory	WMO	0.9 m	Finger Lakes PL-3041-UV	0.″61	21′ × 21′	Jan–July	*BVR*	44
Wise Observatory	WC18	0.5 m	STL-6303E CCD	1.″47	75′ × 50′	Dec–Jul	*BVRI*	126

stars in the subtracted images and rescaled the formal ISIS errors to be consistent with the observed scatter. Our method is similar to that of Hartman et al. (2004, Section 4.1).

We first used ISIS to extract differential light curves at the positions of each unsaturated star in the reference images. For stars with constant flux in time, the distribution of residual fluxes at each epoch serves as an estimate of the uncertainty in the subtraction. Since we are only concerned with the magnitude of the residuals, we first take their absolute value. We then divide these values by their formal ISIS uncertainties, so that the resulting ratios indicate the factor by which the true uncertainties are underestimated. We set a minimum value of 1.0 for this ratio, since the uncertainty cannot be smaller than the local photon noise. Finally, we multiply the formal uncertainty for the AGN at the matching epoch by the median of the rescaling factors from all stars. The procedure ensures that the measurement uncertainty in a given image is consistent with the observed scatter of the subtracted stars. The median rescaling factor for all images was 2.9, while 75% of the rescaling factors are less than 6.6 and 98% are less than 25.0. The remaining 2% have rescaling factors between 30 and 87. The poorest subtractions result when ISIS cannot accurately construct the image PSF, usually because the image has too few stars.

To assess the effectiveness of this method, we adjusted the stars' uncertainties by the derived rescaling factor for each image and then checked the goodness of fit for a constant-flux model of each star. The goodness of fit is calculated by

$$\chi^2/\mathrm{dof} = \frac{1}{N-1}\sum_{i}^{N}\left(\frac{c_i - \bar{c}}{\sigma_i}\right)^2, \quad (1)$$

where $\mathrm{dof} = N - 1$ is the number of degrees of freedom of the fit, c_i is the counts in the light curve at epoch i, σ_i is the rescaled uncertainty, and $\bar{c}$ is the mean counts of the light curve. 90% of the rescaled values of χ^2/dof are between 0.32 and 2.09, and the distribution peaks at 0.81, somewhat lower than would be expected for purely Gaussian statistics. This may indicate that our rescaling method is slightly overestimating the measurement uncertainties. However, given our large data set, we can afford to be conservative in this regard.

Data from the Katzman Automatic Imaging Telescope (KAIT; Filippenko et al. 2001) and the *u*-band data from the Liverpool Telescope (LT; Steele et al. 2004) required a different treatment since these images have 10 stars or fewer, which is not enough to provide robust estimates of the error-rescaling factors. We instead calculated global rescaling factors from all available epochs, rather than individual corrections from single images. Using Equation (1), we calculate χ^2/dof for all available stars, using the unscaled ISIS uncertainties for σ_i. We then multiplied the uncertainties of the AGN light curve by the average value of $(\chi^2/\mathrm{dof})^{1/2}$. We found that the mean rescaling factor was 8.99 for the KAIT data and 2.23 for the *u*-band LT data. Although this method does not account for epochs with high-quality subtractions, we find the cautious approach preferable to underestimating the uncertainties.

2.3. Intercalibration of Light Curves

In order to combine differential light curves in the same filter but from different telescopes, it is necessary to intercalibrate the light curves to a common flux scale. This accounts for the different mean flux levels and analog-to-digital unit (ADU) definitions between the reference images, as well as small differences in filter transmission functions, detector efficiencies, etc., of the many telescopes. We model the difference of any two light curves by a multiplicative rescaling factor a and an additive shift b. While it is trivial to solve for these parameters by matching epochs where the fluxes are known to be equal, no two observations occur at precisely the same time and it is therefore necessary to interpolate the light curves. Furthermore, this method can only treat two light curves at a

time and therefore loses information by ignoring the global probability of the ensemble calibration parameters for all telescopes. In order to address both of these problems, we built a full statistical model of the intercalibrated light curve using the software package JAVELIN, following the SPEAR formalism of Zu et al. (2011).

JAVELIN models the light curves as a damped random walk (DRW). Although recent studies using *Kepler* light curves have shown that the DRW overpredicts the amplitude of AGN continuum variability on short timescales (Edelson et al. 2014; Kasliwal et al. 2015), the DRW provides an adequate description of the observed light curves for the noise properties and cadence/timescales of this study (we quantitatively verify this claim in the Appendix, but see also Kelly et al. 2009; MacLeod et al. 2010; Zu et al. 2013). In brief, points sampled from a DRW have an exponential covariance matrix, which is described by an amplitude $\sigma_{\rm DRW}$ that characterizes the strength of short-term variations and a damping timescale $\tau_{\rm DRW}$ over which the light curve becomes decoherent. Using a Markov Chain Monte Carlo (MCMC) calculation, we simultaneously fit for the shifts and rescaling factors of all light curves in a single filter. We also fit for $\sigma_{\rm DRW}$, but our light curves do not have a sufficiently long temporal baseline to meaningfully constrain $\tau_{\rm DRW}$. We therefore fixed $\tau_{\rm DRW} = 164$ days, so as to match the value determined from multiyear historical light curves of NGC 5548 (Zu et al. 2011). The model provides a well-defined and self-consistent means of interpolating all the light curves simultaneously (see Zu et al. 2011; Li et al. 2013 for further details).

Our fitting procedure requires one light curve to be chosen to define the flux scale and mean flux level of the resulting intercalibration, so that this reference light curve is assigned a shift of 0 and a rescaling factor of 1. In the Johnson *BVRI* bands, we use the Wise C18 (WC18; Brosch et al. 2008) data as the calibration light curve, owing to its dense temporal sampling, long baseline, and large number of comparison stars (>400). For the SDSS *ugriz* bands, we use the LT light curves, since they have the longest baseline and most complete time sampling.

Uncertainty in the intercalibration parameters for a given telescope contributes to the final measurement uncertainty. For a flux measurement $f(t_i)$ at epoch t_i, the calibrated measurement is $f_c(t_i) = af(t_i) + b$, and standard error propagation shows that the uncertainty introduced per point is $\sigma_{f_c}^2 = \sigma_a^2 f(t_i)^2 + \sigma_b^2 + 2f(t_i)\mathrm{cov}(a, b)$. Since a and b are usually anticorrelated, σ_{f_c} is often small compared to the uncertainties from image subtraction. However, this is not always the case for telescopes with very small numbers of observations, so we calculated σ_a, σ_b, and $\mathrm{cov}(a, b)$ from the posterior distributions of these parameters for each telescope and added σ_{f_c} in quadrature to the rescaled ISIS uncertainties for each epoch. This treatment is very conservative, since the intercalibration uncertainty is strongly correlated between points from a single telescope. A summary of the mean intercalibration uncertainties is given in Table 2.

The choice of reference light curves defines the physical flux level of the AGN from the corresponding ISIS reference image (WC18 and LT). We convert the intercalibrated differential light curves to physical flux units by performing aperture photometry on these reference images. For the AGN and all unsaturated stars in the field, we measured the flux enclosed in a 5.″0 radius circular aperture and converted the summed fluxes to instrumental magnitudes. This means that the host-galaxy light within the aperture is included in the measurement of the AGN flux, and this issue is discussed in Section 2.4. The background sky level was estimated from an annulus with inner/outer radius of 14″/29″ for the stars and 118″/132″ for the AGN (so as to avoid light from the host galaxy).

Table 2
Mean Intercalibration Uncertainty

Telecope (Matches Table 1)	*B* (%)	*V* (%)	*R* (%)	*I* (%)	*u* (%)	*g* (%)	*r* (%)	*i* (%)	*z* (%)
WC18	ref	ref	ref	ref	⋯	⋯	⋯	⋯	⋯
LT	⋯	⋯	⋯	⋯	ref	ref	ref	ref	ref
LCOGT1	0.9	0.2	⋯	⋯	1.1	1.2	0.5	0.1	0.3
LCOGT2	2.3	0.4	⋯	⋯	1.8	0.5	1.9	0.4	1.9
LCOGT3	1.5	0.6	⋯	⋯	⋯	⋯	⋯	⋯	⋯
LCOGT4	2.7	⋯	⋯	⋯	⋯	⋯	0.3	0.1	0.2
LCOGT5	⋯	0.6	⋯	⋯	⋯	1.3	⋯	⋯	0.7
LCOGT6	⋯	0.5	⋯	⋯	⋯	1.6	1.4	0.4	⋯
LCOGT7	⋯	1.9	⋯	⋯	⋯	⋯	⋯	⋯	⋯
LCOGT8	⋯	1.3	⋯	⋯	⋯	⋯	⋯	⋯	⋯
WMO	0.9	0.6	0.3	⋯	⋯	⋯	⋯	⋯	⋯
CrAO	0.2	⋯	0.3	0.3	⋯	⋯	⋯	⋯	⋯
RCT	0.2	0.1	⋯	⋯	⋯	⋯	⋯	⋯	⋯
MO15	⋯	0.4	0.7	⋯	⋯	⋯	⋯	⋯	⋯
FWO	⋯	0.3	⋯	⋯	⋯	⋯	⋯	⋯	⋯
HLCO	⋯	0.4	⋯	⋯	⋯	⋯	⋯	⋯	⋯
KAIT	⋯	0.1	⋯	⋯	⋯	⋯	⋯	⋯	⋯
MLO	⋯	0.7	⋯	⋯	⋯	⋯	⋯	⋯	⋯
LOAO	⋯	0.4	⋯	⋯	⋯	⋯	⋯	⋯	⋯

Note. Percentages are averaged for all epochs of the given telescope, measured relative to the flux at that epoch—see Section 2.3 for the definition of the intercalibration uncertainty. "ref" is the reference telescope to which the others are aligned.

We then matched all stars to the SDSS Data Release 7 catalog (Abazajian et al. 2009) and computed the offset between instrumental magnitudes and the SDSS AB magnitudes. We did not find any significant color terms in the flux calibration from the comparison stars, although the spectral slope of the AGN would be a poor match to such color terms regardless of their small values. For the Johnson/Cousins *BVRI* bands, we determined the comparison-star magnitudes using the filter-system transformations given by Fukugita et al. (1996) and converted these to AB magnitudes using Table 8 of Fukugita et al. (1996). The filter transforms have an uncertainty of ~0.03 mag, which we adopt as a floor for the *BVRI* flux-calibration uncertainty. The final flux-calibrated light curves are shown in Figure 1 and given in Table 3.

2.4. Light Curve Properties

Paper I and Paper II only presented the *HST* 1367 Å continuum light curve; here we include three additional UV continuum light curves measured from the *HST* COS spectra, extracted from 5 to 6 Å windows centered at 1158, 1479, and 1746 Å and given in Table 4. These continuum windows were chosen to be as uncontaminated as possible by absorption lines and broad emission-line wings. We also drop the *Swift V*-band light curve from this analysis because its mean fractional uncertainty is much larger than that of the ground-based

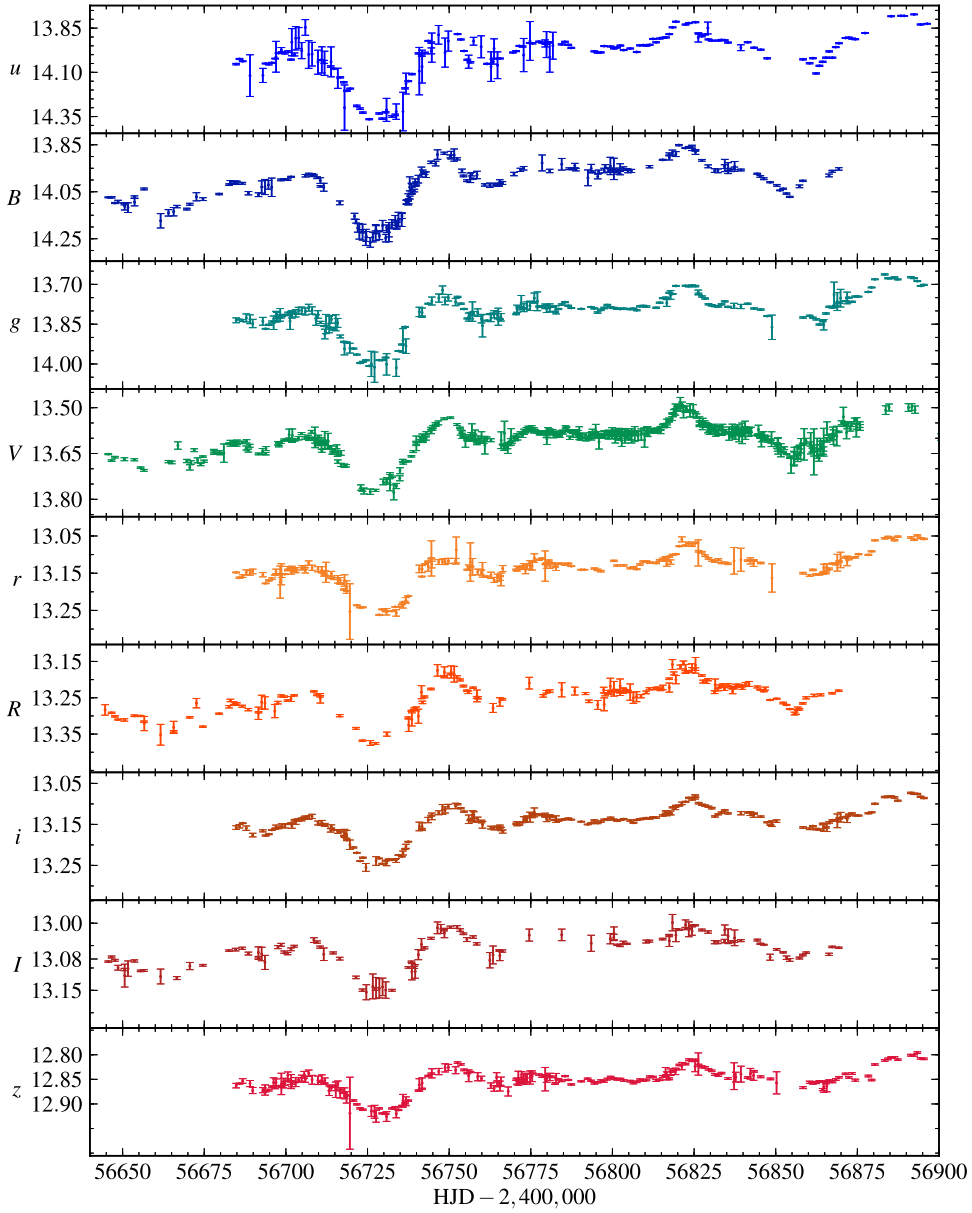

Figure 1. *BVRI* and *ugriz* ground-based light curves from the full monitoring campaign in AB magnitudes. Only the measurement uncertainties in the differential fluxes are shown. These uncertainties include those due to intercalibration, summarized in Table 2. Systematic uncertainties for the absolute flux calibration are given in Table 5.

Johnson *V*-band light curve (3.2% compared to 0.8%). Table 5 gives a summary of the sampling properties of the AGN STORM continuum light curves and shows that the light curves have approximately daily cadence over the entire campaign. The reported wavelengths of the optical light curves are pivot wavelengths calculated from the filter response curves of the optical bands, and they are independent of the source spectrum (atmospheric cutoffs at 3000 Å and 1 μm were imposed for these calculations). Figure 2 shows a comparison of all the continuum light curves used in this study.

Table 5 also gives the variability properties of the light curves. Column (8) gives the mean flux and rms scatter of the light curves, corrected for Galactic extinction assuming a Cardelli et al. (1989) extinction law with $R_V = 3.1$ and $E(B-V) = 0.0171$ mag (Schlegel et al. 1998; Schlafly & Finkbeiner 2011; Paper I). Columns (10), (11), and (12) give different estimates of their fractional variability. The fractional variability $F_{\rm var}$ of a light curve is defined by

$$F_{\rm var} = \frac{1}{\langle f(t)\rangle}\sqrt{\frac{1}{N}\sum_{i}^{N}\{[f(t_i) - \langle f(t)\rangle]^2 - \sigma_i^2\}}\,, \qquad (2)$$

and the uncertainty in $F_{\rm var}$ is

$$\sigma^2_{F_{\rm var}} = \left(\sqrt{\frac{1}{2N}}\frac{\langle\sigma^2\rangle}{\langle f(t)\rangle^2 F_{\rm var}}\right)^2 + \left(\sqrt{\frac{\langle\sigma^2\rangle}{N}}\frac{1}{\langle f(t)\rangle}\right)^2, \qquad (3)$$

where $f(t_i)$ is the value of the light curve at epoch i, σ_i is the associated uncertainty, $\langle f(t)\rangle$ is the (unweighted) mean value of the light curve, and $\langle\sigma^2\rangle$ is the mean square of the measurement uncertainties (Rodríguez-Pascual et al. 1997; Vaughan et al. 2003). We also estimated the fractional variability using the JAVELIN amplitudes, $\sigma_{\rm DRW}/\langle f\rangle$, since

Table 3
Optical Continuum Light Curves

Filter	HJD −2,400,000	F_λ (10^{-15} erg cm^{-2} s^{-1} Å^{-1})	Telescope ID (As in Table 1)	Differential Counts (DC) (Reference Counts)	Error DC (Reference Counts)
u	56,684.78	21.61 ± 0.08	LT	−34,438.0	1292.5
	56,685.79	22.19 ± 0.07	LT	−24,994.0	1050.5
	56,686.77	21.93 ± 0.04	LT	−29,223.0	707.5
	…	…	…	…	…
B	56,645.64	13.39 ± 0.02	WC18	−16,159.0	460.55
	56,646.65	13.40 ± 0.04	WC18	−16,055.0	764.35
	56,647.65	13.10 ± 0.03	WC18	−22,095.0	595.81
	…	…	…	…	…
g	56,684.78	13.96 ± 0.12	LT	−8759.7	1384.1
	56,685.79	14.00 ± 0.02	LT	−8305.6	192.33
	56,686.77	13.95 ± 0.05	LT	−8892.6	579.47
	…	…	…	…	…
V	56,645.62	12.91 ± 0.02	WC18	−4676.7	338.64
	56,646.61	12.66 ± 0.03	WC18	−8876.5	500.65
	56,647.63	12.79 ± 0.03	WC18	−6668.4	524.11
	…	…	…	…	…
r	56,684.78	15.73 ± 0.01	LT	−16,832.0	491.06
	56,685.79	15.52 ± 0.03	LT	−23,984.0	915.05
	56,686.77	15.59 ± 0.05	LT	−21,698.0	1786.4
	…	…	…	…	…
R	56,644.64	12.76 ± 0.17	CrAO	−7835.7	4544.9
	56,646.63	12.67 ± 0.02	WC18	−10,378.0	588.18
	56,647.64	12.56 ± 0.02	WC18	−13,352.0	585.57
	…	…	…	…	…
i	56,684.78	10.16 ± 0.04	LT	−14,639.0	2267.2
	56,685.78	10.19 ± 0.04	LT	−13,055.0	2074.4
	56,686.77	10.26 ± 0.01	LT	−9307.6	458.99
	…	…	…	…	…
I	56,645.63	8.67 ± 0.01	WC18	−6575.6	499.37
	56,646.63	8.75 ± 0.02	WC18	−3043.8	732.31
	56,647.64	8.69 ± 0.02	WC18	−5582.9	702.53
	…	…	…	…	…
z	56,684.78	9.30 ± 0.04	LT	−4697.2	984.0
	56,685.78	9.34 ± 0.01	LT	−3818.5	197.04
	56,686.77	9.38 ± 0.04	LT	−2659.7	1013.4

(This table is available in its entirety in machine-readable form.)

Table 4
HST Continuum Light Curves

Wavelength (Å)	HJD −2,400,000	F_λ (10^{-15} erg cm^{-2} s^{-1} Å^{-1})
1157.5	56,690.61	32.40 ± 0.89
	56,691.54	34.80 ± 0.92
	56,692.39	37.50 ± 0.95
	…	…
1367.0	56,690.61	34.27 ± 0.64
	56,691.54	35.45 ± 0.65
	56,692.39	37.71 ± 0.67
	…	…
1478.5	56,690.65	29.70 ± 0.48
	56,691.58	31.60 ± 0.51
	56,692.41	33.00 ± 0.52
	…	…
1746.0	56,690.65	26.70 ± 0.63
	56,691.58	27.90 ± 0.64
	56,692.41	30.40 ± 0.68

(This table is available in its entirety in machine-readable form.)

this is an equivalent measure of $F_{\rm var}$ under the DRW model. The values of $\sigma_{\rm DRW}/\langle f \rangle$ and $F_{\rm var}$ are often in good agreement, but with notable exceptions, as given in Table 5.

Figure 3 shows the mean flux and variability properties of these light curves. The top panel displays the mean SED (corrected for Galactic extinction). The vertical error bars show the minimum and maximum states of the AGN, which occur at HJD –2,400,000 = 56,723.1 and 56,818.9, respectively. These dates are based on the *HST* 1367 Å light curve, and the other bands are adjusted for interband time delays that are measured in Section 3. The middle panel illustrates the logarithm of the difference in flux between the minimum and maximum states of the AGN, which cleanly isolates the variable component of the spectrum and better traces the shape of the accretion-disk SED. For comparison, a standard thin accretion disk SED with $\lambda F_\lambda \propto \lambda^{-4/3}$ is shown, arbitrarily normalized to match the Johnson *V*-band differential flux. Although the data are in excellent agreement with the prediction at longer wavelengths, the UV data lie significantly below the model SED. This discrepancy may be caused by extinction internal to the AGN, or the inner edge of the disk, which will display an exponential

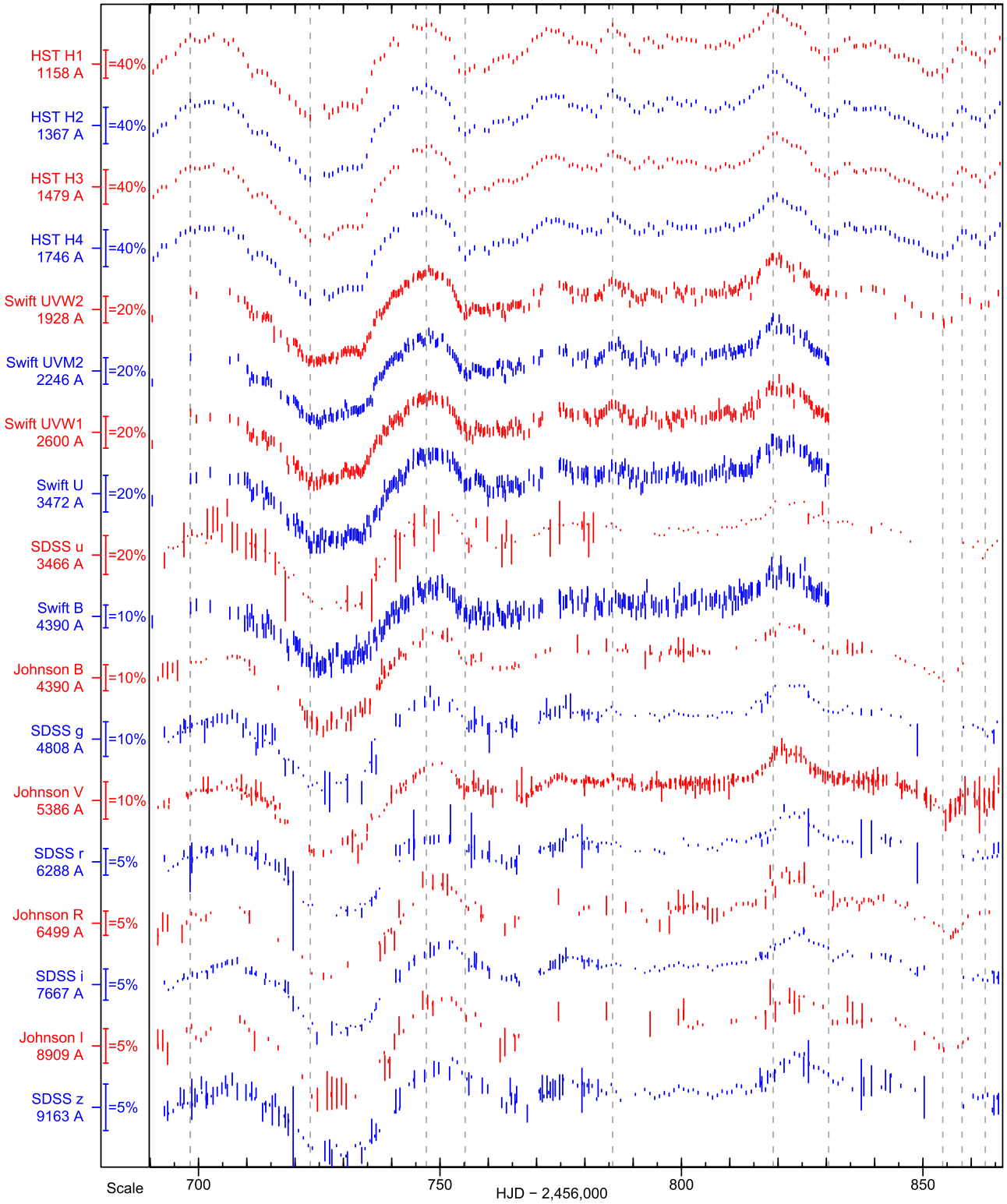

Figure 2. AGN STORM UV and optical continuum light curves used in this analysis, restricted to the observing window of the *HST* campaign. Light curves have been converted to AB magnitudes but are rescaled and shifted for clarity—the scales along the vertical axis show the fractional variations. The vertical dashed lines mark local extrema in the *HST* 1158 Å light curve.

Wien cutoff rather than $\lambda F_\lambda \propto \lambda^{-4/3}$. A more complete discussion and modeling of the variable spectrum will be presented by D. A. Starkey et al. (2016, in preparation). Finally, the bottom panel shows $F_{\rm var}$ as a function of wavelength. The far-UV light curves have values of $F_{\rm var} \geqslant 0.20$, which sharply decrease with wavelength to about 0.06 in the V band. At longer wavelengths, the trend flattens, reaching 0.02 in the z band.

At least part of this effect is caused by the constant flux contributed by the host galaxy, which becomes increasingly

Table 5
Light Curve Properties

Source	Filter	$\lambda_{\rm pivot}$ (Å)	Flux Calibration Uncertainty (mag)	$N_{\rm obs}$	$\Delta t_{\rm ave}$ (days)	$\Delta t_{\rm med}$ (days)	$\langle f(t)\rangle$[a]	Host[a]	$F_{\rm var}$	$F_{\rm var2}$[b]	$\sigma_{\rm DRW}/\langle f(t)\rangle$
(1)	(2)	(3)	(4)	(5)	(6)	(7)	(8)	(9)	(10)	(11)	(12)
HST	λ1158	1158	0.050	171	1.03	1.00	52.41 ± 13.38	⋯	0.254 ± 0.002	0.254 ± 0.002	0.281 ± 0.054
HST	λ1367	1367	0.050	171	1.03	1.00	49.17 ± 9.89	⋯	0.200 ± 0.001	0.200 ± 0.001	0.205 ± 0.062
HST	λ1479	1479	0.050	171	1.03	1.00	43.54 ± 9.20	⋯	0.211 ± 0.001	0.211 ± 0.001	0.176 ± 0.029
HST	λ1746	1746	0.058	171	1.03	1.00	38.26 ± 7.32	⋯	0.190 ± 0.002	0.190 ± 0.002	0.145 ± 0.024
Swift	*UVW2*	1928	0.030	284	0.62	0.39	34.71 ± 5.83	⋯	0.166 ± 0.001	0.166 ± 0.001	0.150 ± 0.023
Swift	*UVM2*	2246	0.030	256	0.55	0.35	33.83 ± 5.55	⋯	0.162 ± 0.002	0.162 ± 0.002	0.121 ± 0.017
Swift	*UVW1*	2600	0.030	270	0.52	0.38	29.70 ± 4.01	⋯	0.133 ± 0.002	0.133 ± 0.002	0.097 ± 0.014
Swift	*U*	3467	0.020	145	1.20	0.99	24.43 ± 2.59	1.22 ± 0.02	0.104 ± 0.002	0.110 ± 0.002	0.236 ± 0.021
Ground	*u*	3472	0.035	270	0.52	0.38	23.18 ± 2.94	1.16 ± 0.02	0.124 ± 0.002	0.130 ± 0.002	0.068 ± 0.012
Ground	*B*	4369	0.030	151	1.11	0.98	15.15 ± 1.36	2.88 ± 0.05	0.089 ± 0.001	0.110 ± 0.001	0.090 ± 0.007
Swift	*B Swift*	4392	0.016	271	0.52	0.37	15.69 ± 1.48	2.98 ± 0.05	0.090 ± 0.002	0.112 ± 0.002	0.019 ± 0.003
Ground	*g*	4776	0.034	172	1.01	0.97	15.06 ± 0.89	3.83 ± 0.08	0.058 ± 0.001	0.078 ± 0.001	0.081 ± 0.005
Ground	*V*	5404	0.030	429	0.41	0.31	14.29 ± 0.56	4.79 ± 0.10	0.039 ± 0.001	0.058 ± 0.001	0.112 ± 0.007
Ground	*r*	6176	0.032	172	1.01	0.93	16.49 ± 0.59	5.76 ± 0.12	0.035 ± 0.001	0.054 ± 0.001	0.059 ± 0.005
Ground	*R*	6440	0.030	136	1.28	0.96	13.88 ± 0.52	5.25 ± 0.10	0.037 ± 0.001	0.060 ± 0.001	0.049 ± 0.003
Ground	*i*	7648	0.021	178	0.98	0.96	10.59 ± 0.33	5.33 ± 0.10	0.031 ± 0.001	0.063 ± 0.001	0.032 ± 0.002
Ground	*I*	8561	0.030	98	1.73	1.02	9.15 ± 0.32	4.73 ± 0.08	0.034 ± 0.001	0.071 ± 0.001	0.030 ± 0.002
Ground	*z*	9157	0.011	186	0.93	0.91	9.57 ± 0.21	5.00 ± 0.08	0.021 ± 0.001	0.044 ± 0.001	0.019 ± 0.002

Notes. $N_{\rm obs}$ gives the number of epochs in the light curve, $\Delta t_{\rm ave}$ gives the average cadence, $\Delta t_{\rm med}$ gives the median cadence, $\langle f(t)\rangle$ gives the mean flux (the uncertainty gives the rms scatter of the light curve), "Host" gives the host-galaxy flux, $F_{\rm var}$ is defined in Section 2.4, and $\sigma_{\rm DRW}$ is the DRW amplitude. The flux calibration uncertainty is the systematic uncertainty for conversion to physical units (i.e., zero-point errors). For *HST*, these values are taken from Paper I, while for *Swift* the values are from Table 6 of Poole et al. (2008). The uncertainties for the ground-based light curves represent our calibration to the SDSS AB mag photometric system. A correction for Galactic extinction has been applied to these data (see Section 2.4 for details).
[a] 10^{-15} erg cm^{-2} s^{-1} Å^{-1}.
[b] Corrected for host-galaxy flux.

important at longer wavelengths. Based on spectral decomposition models and synthetic photometry (described in Sections 4.1 and 4.2), the host galaxy contributes about 20% of the observed flux in the *B* band and about 54% in the *I* and *z* bands. We corrected $\langle f(t)\rangle$ for this constant component, and Figure 3 and Table 5 also show the host-galaxy flux and revised values of $F_{\rm var}$. The effect on the trend in Figure 3 is fairly subtle and does not change the flattening at optical wavelengths.

The larger variability amplitudes at short wavelengths suggest that the SED of NGC 5548 becomes bluer in higher flux states. The same effect was seen by Cackett et al. (2015) in NGC 5548 with near-UV grism monitoring data from *Swift*. However, the trend is driven by the light curves at wavelengths <5000 Å and is most significant at wavelengths $\lesssim$3500 Å, which may be why optical studies of AGN variability do not always find any "bluer when brighter" trend (e.g., Sakata et al. 2010).

3. TIME-SERIES ANALYSIS

We measure the lags between light curves using two methods. First, we use the interpolated cross-correlation function (ICCF), as employed by Peterson et al. (2004), and estimate the uncertainty of the lag using a Monte Carlo method. Second, we use `JAVELIN`, which measures lags by modeling reverberating light curves as shifted, scaled, and smoothed versions of the driving light curve.

In the first method, the ICCF is calculated by shifting one light curve on a grid of lags τ spaced by 0.1 days and calculating the correlation coefficient $r_{\rm cc}(\tau)$ by linearly interpolating the second light curve. The lags are estimated from the centroid of the ICCF, defined as the mean ICCF-weighted lag for which $r_{\rm cc}(\tau) > 0.8 r_{\rm max}$. Uncertainties are estimated using the flux randomization/random subset selection (FR/RSS) method, wherein a distribution of ICCF centroids is built from cross-correlating 10^3 realizations of both light curves. Each realization consists of randomly selected epochs (chosen with replacement), and the corresponding flux measurements are adjusted by random Gaussian deviates scaled to the measurement uncertainties. The lags reported here correspond to the medians of the ICCF centroid distributions, while the lower and upper uncertainties define their central 68% confidence intervals.

We detrended the light curves, as is common practice in RM studies (Peterson et al. 2004; Paper II), in order to remove long-term secular trends that are poorly sampled in the frequency domain and may bias the observed lag (Welsh 1999). The detrending procedure consists of subtracting a second-order polynomial linear least-squares fit (with equal weight given to all data points) from the observed light curves. Following Paper I and Paper II, we restricted the analysis to the time period coincident with the *HST* campaign and measured the time delays relative to the *HST* 1367 Å light curve. When calculating the ICCF, we only interpolate the 1367 Å light curve. Table 6 summarizes the resulting mean lags, corrected for cosmological time dilation (the redshift of NGC 5548 is $z = 0.017175$; Paper I). Lags for the hard and soft X-ray bands of the *Swift* XRT are also included, as determined in Paper II. The ICCF for all bands is shown in Figure 4 with the solid

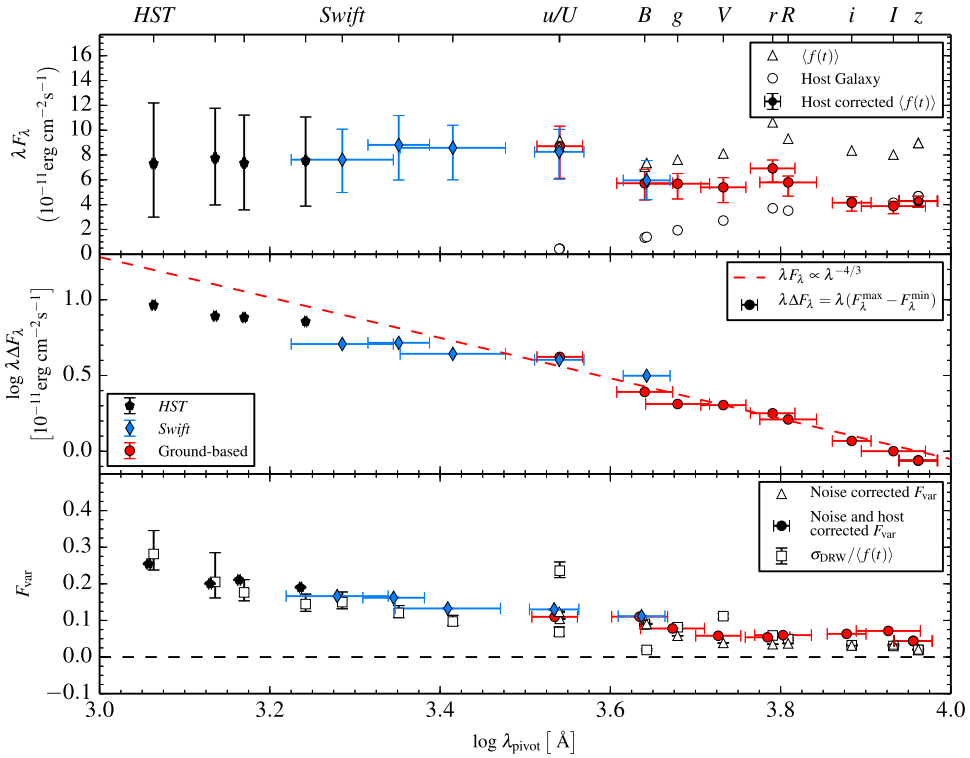

Figure 3. Top panel: mean SED of NGC 5548 from far-UV to optical wavelengths, corrected for Galactic extinction. The vertical error bars represent the AGN in the maximum and minimum states of the campaign. The horizontal error bars represent the rms width of the filter transmission curves. See Section 4 for a discussion of the host-galaxy estimate. Middle panel: variable SED component, calculated from the difference in flux between the minimum and maximum states, which more cleanly identifies the accretion-disk spectrum. The dashed red line is the predicted spectrum for a standard thin disk—discrepancies at short wavelengths may be due to extinction internal to the AGN or the inner edge of the disk. Bottom panel: fractional variability $F_{\rm var}$ as a function of wavelength. $\sigma_{\rm DRW}$ is the DRW amplitude from the JAVELIN fits. For clarity, a small shift in wavelength to the $F_{\rm var}$ points has been applied.

black lines, while the centroid distributions are shown as the gray histograms. We found that the *HST* 1158 and 1479 Å lags were only slightly larger than the spacing of our interpolation grid (0.1 days), so we repeated the procedure on these light curves using a grid of 0.01 days. This did not have a noticeable effect on the ICCF centroids, but it did change the ICCF peaks by ∼0.05 days. The lags reported in Table 6 make use of the finer grid for these light curves.

Our treatment of the *Swift* light curves (*UVW2*, *UVM2*, *UVW1*, *U*, and *B*) results in lags systematically larger than those found in Paper II, although the tension is only moderate (typically $\lesssim 1.5\sigma$). These differences are primarily caused by the different detrending procedures of the two studies. Paper II detrended the *Swift* light curves using a 30-day running mean, while we use a low-order polynomial. A running mean removes more low-frequency power than a polynomial trend, and is therefore expected to result in smaller lags. However, several of our light curves have very irregular sampling, which makes the calculation of the running mean poorly defined, so we instead use the low-order polynomial. The ground-based SDSS *u* and *Swift U* lags and the Johnson *B* and *Swift B* lags are consistent at the $\sim 0.6\sigma$ level using the polynomial detrending, so it is likely that the detrending procedure accounts for most of the difference between the near-UV lags. Two other smaller effects may be important for the lag determinations. First, the *Swift* UVOT optical filters are much narrower than the standard Bessell filters used for the ground-based light curves, so the observed variations are not perfectly identical (the *Swift* light curves also have slightly shorter baselines). Second, the *Swift* optical light curves have much larger fractional uncertainties, which may shift the ICCF centroid distribution of the otherwise similar light curves.

We also estimate the lags using JAVELIN, which calculates a maximum-likelihood lag, scale factor, and kernel width (assuming a top-hat transfer function) from the DRW covariance matrices. JAVELIN internally employs a linear detrending procedure, so we do not apply the second-order detrending as for the ICCF analysis. We also imposed a minimum kernel width of 0.75 days, in order to suppress solutions where JAVELIN finds a δ-function transfer function and aligns the reverberating light curve with the gaps between samples of the driving light curve (this is an aliasing problem associated with light curves that have similar cadences).

We adopt the medians of the posterior lag distributions and their central 68% confidence intervals as estimates of the lag and its uncertainty, which are given in Table 6. The posterior distributions are shown by the red histograms in Figure 4. The median lags are always consistent with the ICCF analysis, with the largest discrepancy being 1.7σ in the *r* band. The Javelin uncertainties generically appear to be uncomfortably small. This is because JAVELIN assumes correctly characterized random Gaussian measurement errors, that the line light curve is a simple lagged and smoothed version of the continuum light curve, and that the smoothing kernel is well characterized by the functional form of the model (a top-hat function). Given that all these requirements are seldom fully met (particularly the Gaussianity of the measurement errors), Javelin uncertainties need to be interpreted conservatively. A rough

Table 6
Time Delays

Source	Filter	$\lambda_{\rm pivot}$ (Å)	ICCF $\tau_{\rm cent}$ (days)	ICCF $\tau_{\rm peak}$ (days)	ICCF $r_{\rm max}$	JAVELIN $\tau_{\rm JAV}$ (days)
Swift	HX	4.4	$-0.65^{+0.45}_{-0.45}$	$-0.46^{+0.49}_{-0.39}$	0.35 ± 0.20	⋯
Swift	SX	25.3	$0.08^{+0.51}_{-0.51}$	$0.23^{+0.29}_{-0.39}$	0.44 ± 0.07	⋯
HST	λ1158	1158	$-0.17^{+0.16}_{-0.16}$	$-0.21^{+0.08}_{-0.10}$	1.07 ± 2.53	$-0.14^{+0.04}_{-0.04}$
HST	λ1479	1479	$0.15^{+0.18}_{-0.16}$	$0.14^{+0.23}_{-0.06}$	1.03 ± 1.08	$0.03^{+0.04}_{-0.04}$
HST	λ1746	1746	$0.22^{+0.16}_{-0.19}$	$0.21^{+0.10}_{-0.10}$	0.98 ± 0.01	$0.14^{+0.05}_{-0.05}$
Swift	*UVW2*	1928	$0.63^{+0.19}_{-0.18}$	$0.59^{+0.20}_{-0.10}$	0.92 ± 0.16	$0.68^{+0.11}_{-0.09}$
Swift	*UVM2*	2246	$0.68^{+0.19}_{-0.20}$	$0.59^{+0.20}_{-0.10}$	0.90 ± 0.27	$0.69^{+0.14}_{-0.17}$
Swift	*UVW1*	2600	$0.93^{+0.20}_{-0.23}$	$0.88^{+0.29}_{-0.20}$	0.89 ± 0.01	$0.90^{+0.16}_{-0.16}$
Swift	*U*	3467	$1.80^{+0.24}_{-0.24}$	$1.47^{+0.20}_{-0.29}$	0.88 ± 0.35	$1.62^{+0.16}_{-0.16}$
Ground	*u*	3472	$2.03^{+0.43}_{-0.39}$	$2.04^{+0.29}_{-0.39}$	0.83 ± 0.04	$1.90^{+0.04}_{-0.04}$
Ground	*B*	4369	$1.42^{+0.36}_{-0.33}$	$1.22^{+0.20}_{-0.29}$	0.91 ± 0.02	$1.36^{+0.11}_{-0.13}$
Swift	*B*	4392	$1.64^{+0.31}_{-0.27}$	$1.28^{+0.29}_{-0.39}$	0.82 ± 0.02	$1.34^{+0.19}_{-0.21}$
Ground	*g*	4776	$1.98^{+0.34}_{-0.29}$	$1.64^{+0.29}_{-0.39}$	0.89 ± 0.02	$1.45^{+0.06}_{-0.04}$
Ground	*V*	5404	$2.04^{+0.22}_{-0.20}$	$1.87^{+0.29}_{-0.10}$	0.84 ± 0.02	$1.72^{+0.07}_{-0.07}$
Ground	*r*	6176	$3.13^{+0.41}_{-0.46}$	$3.12^{+0.29}_{-0.59}$	0.85 ± 0.04	$2.38^{+0.06}_{-0.07}$
Ground	*R*	6440	$3.22^{+0.30}_{-0.29}$	$2.88^{+0.39}_{-0.20}$	0.87 ± 0.11	$2.81^{+0.04}_{-0.05}$
Ground	*i*	7648	$3.99^{+0.29}_{-0.29}$	$3.90^{+0.20}_{-0.29}$	0.90 ± 0.02	$3.46^{+0.11}_{-0.08}$
Ground	*I*	8561	$3.59^{+0.53}_{-0.54}$	$2.88^{+0.59}_{-0.88}$	0.86 ± 0.06	$3.38^{+0.07}_{-0.07}$
Ground	*z*	9157	$3.93^{+0.44}_{-0.40}$	$3.71^{+0.59}_{-0.20}$	0.84 ± 0.04	$3.88^{+0.08}_{-0.06}$

Note. Measured relative to the *HST* 1367 Å light curve and corrected to the rest frame. The *Swift* lags are recalculated from Paper II using a second-order polynomial detrending routine, as described in Section 3.

rule of thumb from modeling gravitational lens time delays is that repeated measurements for the same system will typically be within $2\sigma-3\sigma$ of each other.

The very small JAVELIN uncertainties may also indicate that the simple lagged and smoothed model of the reverberating light curve model is an inadequate description of the data. Paper I found a similar result, where the shape of the line light curves was not always a good match to the observed continuum light curve. Therefore, smoothing the continuum light curve by a simple transfer function cannot always reproduce the line light curve, suggesting that other processes are important for the observed line emission (perhaps, for example, anisotropic emission/reprocessing). A more detailed investigation of this result will be pursued in upcoming papers of this series.

Using either lag estimation technique, we find that longer-wavelength continuum variations follow those at shorter wavelengths. Figure 5 shows the lags as a function of the pivot wavelength of each filter. While the far-UV and near-UV light curves have time delays $\tau < 1$ day, the *V* band lags the 1367 Å continuum by 2.04 ± 0.21 days, and the *z* band lags it by 3.93 ± 0.42 days. For comparison, the He II UV and optical lines (1640 and 4686 Å, respectively) have a mean lag of ~2.5 days relative to the 1367 Å light curve (Paper I; Paper V). The optical light curves have a time delay comparable to, and frequently larger than, that of high-ionization-state lines in the BLR.

The trend of larger lags at longer wavelengths is nearly monotonic. The most notable exceptions are (1) in the longest-wavelength filters, where the trend appears to level out near the *i* band, and (2) in the *u* and *U* bands. The *u* and *U* bands have mean lags of 2.03 ± 0.41 days and 1.80 ± 0.24 days, respectively, comparable to or larger than the lags of the *g*- and *V*-band light curves. This may be due to emission originating in the BLR picked up in the *u*- and *U*-band filters, which would contaminate measurements of the AGN continuum emission and artificially increase the observed lag. A similar explanation may exist for the downturn at the *I* and *z* bands, since Paschen continuum emission from the BLR begins at 8204 Å (see Korista & Goad 2001). We return to the question of BLR contamination in Section 4.

Optical continuum lags in NGC 5548 have previously been measured by Sergeev et al. (2005), and the same light curves were reexamined by Chelouche & Zucker (2013) and Chelouche (2013). Sergeev et al. (2005) found substantially longer time delays between the *B* and *R*/Cousins *I* bands than the lags presented here (about 8 days). However, the Sergeev et al. (2005) light curves have ~3-day cadence and suffer from large seasonal/scheduling gaps of 20 days or more. The difference in the optical lags is therefore likely caused by systematic issues with the Sergeev et al. (2005) light curves, such as unfortunate gaps that affect the cross-correlation functions. On the other hand, Chelouche & Zucker (2013) and Chelouche (2013) claim that the large optical lags are due to BLR contamination and that the true continuum lags are consistent with zero. We discuss this possibility further in Section 4.3, but we find this interpretation to be unlikely. These studies did not discuss the impact of gaps in the data on the multivariate cross-correlation function used to disentangle line and continuum lags, and we are further skeptical that this method can meaningfully measure lags below the cadence of the light curves (3 days, in this case).

To avoid the systematics associated with small lags, interband continuum lags should be measured with data taken near or well below the timescale of any suspected lags. The UV wavelength coverage of the STORM project therefore lends a tremendous boost to our ability to detect the continuum lags,

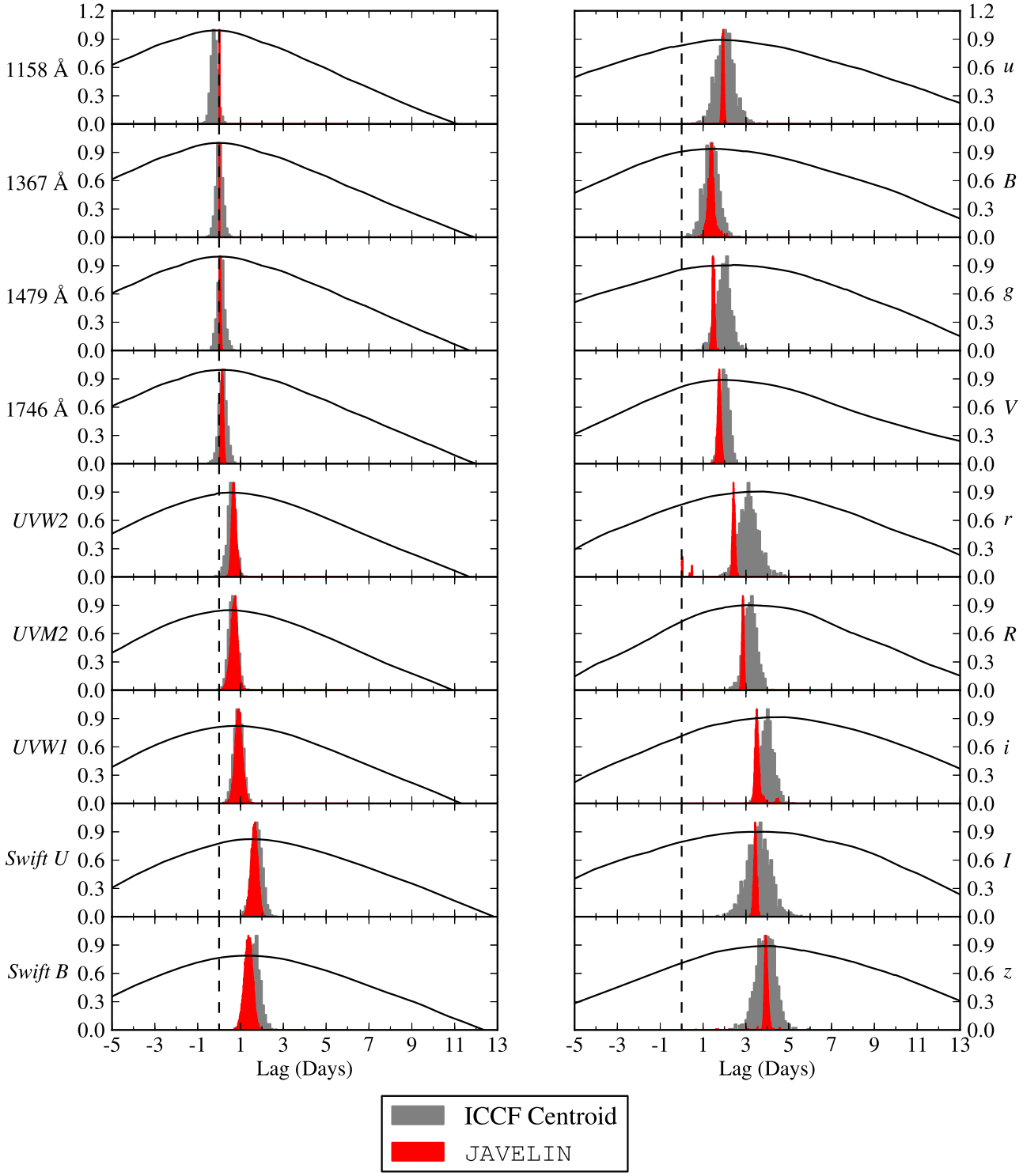

Figure 4. ICCF for all light curves, with the ordinate showing the correlation coefficient r_{cc}. Lags for data from Paper I and Paper II (following our reanalysis) are shown in the left column; ground-based optical lags are presented in the right column. The gray histograms are the ICCF centroid distributions from the FR/RSS method; the red histograms are from JAVELIN. Both histograms are in units of $P(\tau)/\max[P(\tau)]$.

since the UV–optical lags are 3–6 times larger than the interband optical lags. This has implications for ground-based studies attempting to resolve interband continuum lags. Since the optical lags are of order 1 day (or less), the diurnal cycle may make it impossible to measure reliable interband optical lags from the ground without favorable conditions.

In order to quantify the trend of lag with wavelength, we fit a model to the data presented in Figure 5 using the functional form

$$\tau = \alpha\left[\left(\frac{\lambda}{\lambda_0}\right)^{\beta} - 1\right], \quad (4)$$

where τ is the observed lag, λ_0 is a reference wavelength, and α and β are free parameters. As in Paper II, we set $\lambda_0 = 1367$ Å and report all covariances between parameters. The results of

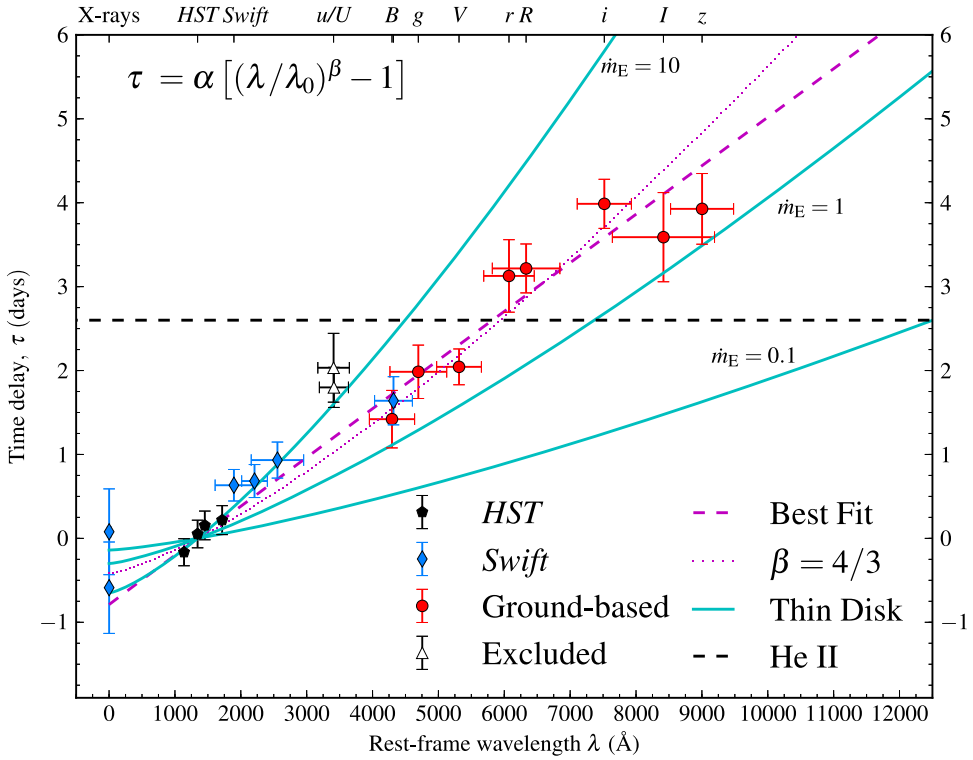

Figure 5. Time delay (ICCF centroid) as a function of pivot wavelength of the filters. The horizontal error bars represent the rms width of the filters. The best-fit model is shown by the dashed magenta line, while the fit fixing $\beta = 4/3$ is shown by the dotted magenta line. Predictions for a thin-disk model with $\dot{m}_E = L/L_{Edd}$ are shown by the solid cyan lines, although the assumptions of the model are unlikely to hold at large $\dot{m}_E$ (see Section 5.3). The mean lag of the He II λλ1640, 4686 lines is shown by the horizontal dashed black line (Paper I; Paper V).

the fits are summarized in Table 7. We find that $\alpha = 0.97 \pm 0.24$ days and $\beta = 0.90 \pm 0.12$. The parameters are strongly correlated, with a normalized correlation coefficient $\rho(\alpha, \beta) = -0.99$, and $\chi^2 = 25.94$, which approaches a low probability for 18 degrees of freedom ($\chi^2/\mathrm{dof} = 1.44$ and $P(\chi^2|\mathrm{dof}) = 0.05$ for a one-tailed χ^2 test). Since there is good reason to suspect that the *u* and *U* bands are affected by BLR emission (see Section 4), we also fit the data excluding these lags. With these bands excluded, we find $\alpha = 0.79 \pm 0.22$ days and $\beta = 0.99 \pm 0.14$. The normalized correlation coefficient does not change, but the goodness of fit is now $\chi^2 = 16.85$ with dof = 16, and $\chi^2/\mathrm{dof} = 1.05$ (and $P(\chi^2|\mathrm{dof}) = 0.60$ for the same one-tailed test). The interpretation of Equation (4) is discussed in Section 5.3.

Table 7
Parameters for Lag–Wavelength Fits

Model	α (days)	β	ρ(α, β)	χ^2	χ^2/dof
All	0.97 ± 0.24	0.90 ± 0.12	−0.99	25.94	1.44
	0.43 ± 0.02	4/3		38.66	2.03
No *Uu*	0.79 ± 0.22	0.99 ± 0.14	−0.99	16.85	1.05
	0.42 ± 0.02	4/3		22.64	1.33
No *UuIR*	0.58 ± 0.20	1.18 ± 0.19	−0.99	12.4	0.89
	0.45 ± 0.02	4/3		13.0	0.87

4. CONTAMINATION BY BLR EMISSION

As noted above, the *u* and *U* lags are outliers from the trend in Figure 5. A major component of the flux observed in these filters is the "small blue bump," caused by bound–bound and bound–free hydrogen emission (the so-called Balmer continuum), as well as blended Fe II lines that originate in the BLR. This BLR emission may cause the *u* and *U*-band lags to be biased estimators of the light-crossing time within the continuum source. In fact, several filters pick up other spectral features that originate in the BLR. The strongest is the prominent Hα line in the *r* and *R* bands, although additional emission lines and a diffuse continuum consisting of bound–free, free–free, electron scattering, and reflection is expected to be present at all wavelengths (Korista & Goad 2001). Understanding the impact of BLR emission on the observed lags is therefore important for interpreting the interband time delays.

In this section, we assess the effect of BLR emission on the interband continuum lags. First, we decompose spectra of NGC 5548 into models of each emission component. We then estimate the fractional contribution from BLR emission in each filter using synthetic photometry. Finally, we simulate broadband filter observations by combining mock continuum and BLR light curves, and we search for biases in the lags by cross-correlating each emission component with the 1367 Å light curve.

4.1. Spectral Decomposition

We begin by decomposing spectra of NGC 5548 into models of each emission component. We obtained moderate-resolution ($R \approx 2000$) optical spectra of NGC 5548 using the Multi-Object Double Spectrographs (MODS; Pogge et al. 2010) on the Large Binocular Telescope (LBT; Hill et al. 2010). These observations are from 2014 June 08 and 25 UT

(HJD = 2,456,817 and 2,456,834, respectively). The spectra were reduced and flux-calibrated using the `modsIDL` Spectral Reduction Pipeline.[66] The spectra cover the wavelength range from 3000 Å to 1 μm. Wavelength solutions were derived from comparison-lamp calibrations for each observing run. Relative-flux calibration was performed using three standard stars observed on the same nights as NGC 5548; however, the observations were taken in poor atmospheric conditions, making their absolute flux calibration unreliable. We therefore rescaled the spectra so that the integrated [O III] λ5007 fluxes match the value measured for the photometric nights of the optical spectral RM campaign, $(5.01 \pm 0.11) \times 10^{-13}$ erg s^{-1} cm^2 (Paper V). The slit width and extraction window of the MODS spectra were 5″ and 15″, respectively, chosen to match those of the optical monitoring spectra. This ensures that the relative contributions of host-galaxy light, narrow-line emission, and BLR emission are the same in both data sets. We corrected for Galactic extinction following the prescription described in Section 2.4. We did not make any correction for telluric absorption because broadband filters suffer from the same effect.

Since we are only concerned with the relative magnitude of various emission components to the broadband filter fluxes, we employed a minimal spectral decomposition, which is relatively coarse compared to state-of-the-art spectral modeling. Accordingly, we do not interpret any of our model parameters as indicative of physical conditions within the AGN, and instead we focus on finding a model that provides a good fit to the data (based on minimizing χ^2). Our decomposition has three components: host-galaxy starlight, the underlying AGN continuum, and the Balmer continuum shortward of ~3648 Å (rest frame). We ignore the diffuse continuum at other wavelengths, since it is poorly constrained, while the Balmer continuum can be determined from the shape and amplitude of the small blue bump. Emission-line fluxes are then estimated by subtracting the summed model components from the observed spectrum.

We simultaneously fit each component with an MCMC calculation, masking AGN emission lines and telluric absorption. We also masked the long and short edges of the spectra, because the MODS flux calibration is unreliable at $\lambda < 3200$ Å and $\lambda > 9100$ Å (rest frame). At these wavelengths, we set the observed flux equal to the summed model, which implicitly sets the emission-line flux to zero. This has a small effect on the estimated BLR contamination in the *u*, *U*, *I*, and *z* bands but is more robust than using the unreliable flux calibration.

Details of the model components are as follows:

1. *Host Galaxy:* We determined the host-galaxy spectrum using the `STARLIGHT` spectral synthesis code (Cid Fernandes et al. 2004). `STARLIGHT` fits the observed spectrum with a linear combination of a large library of synthetic stellar populations that span a wide range of ages and metallicities (150 templates from Bruzual & Charlot 2003). The best-fitting models consist of several very old (usually $>10^{10}$ yr) stellar populations at a range of metallicities (0.4–2.5 $Z_\odot$) and provide a reasonable match to the galaxy templates used by Denney et al. (2010) and Mehdipour et al. (2015). The resulting host templates have one parameter, the flux normalization. We also impose a tight prior on the flux at 5100 Å (rest frame), chosen to match the value measured by Bentz et al. (2013) adjusted to the MODS slit width and extraction window, $(4.52 \pm 0.45) \times 10^{-15}$ erg s^{-1} cm^2 Å^{-1}.
2. *Power Law:* A broken power law is used to model the AGN continuum emission. This component has four free parameters: a flux-normalization factor, two spectral indices, and the location of the transition between indices. A loose prior (a Gaussian distribution with mean 5700 Å and width 700 Å) is imposed on the transition wavelength, to prevent it from moving to the edges of the spectra.
3. *Balmer Continuum:* The Balmer continuum component is estimated from a grid of models calculated by Dietrich et al. (2002), evaluated at varying temperatures, electron densities, and optical depths. Again, we simply choose the template that produces the overall minimum value of χ^2. The templates have a single parameter, a flux rescaling factor.

We ignored blended Fe II emission, because Fe emission is relatively weak in NGC 5548 (Denney et al. 2009; Mehdipour et al. 2015) and varies with an amplitude <50%–75% that of Hβ (Vestergaard & Peterson 2005). This component is therefore expected to contribute very little flux to the broadband photometric measurements and have a negligible impact on the observed lag. In order to assess the effect of this omission, we also fit the spectra with the small blue bump template of Mehdipour et al. (2015), which includes blended Fe II emission lines. We found that these templates produce a poorer fit than the Dietrich et al. (2002) templates at the blue end of the spectrum, which may be a result of the limited wavelength coverage of our MODS spectra in the near-UV.

Each epoch was fit independently, and the resulting component parameters are in reasonable agreement, after allowing for the intrinsic variability of the power-law and Balmer continuum. The flux rescaling factors of the power-law continuum and galaxy templates are degenerate, so the prior imposed on the host-galaxy flux at 5100 Å (rest frame) does the most to constrain these parameters. Figure 6 shows an example of the decomposition, using the spectrum from 2014 June 08, overlaid with the filter transmission curves.

4.2. Synthetic Photometry

Next, we estimate the contribution of each model component to the observed flux in each broadband filter. We first reapply Galactic reddening to the model components, since differential extinction may affect the integrated flux across broadband filters. We then calculate the observed flux using the `synphot IRAF` task and filter transmission curves for the calibration telescopes (WC18 *BVRI* filters and LT *ugriz* filters), truncated at 3000 Å and 1 μm to represent the atmospheric transmission cutoff. Uncertainties in the broadband fluxes of individual components were estimated by resampling the posterior distributions of the model component parameters and rerunning `synphot` 10^3 times.

Table 8 shows the results of our synthetic photometry. The "Total" column was calculated from the original spectrum, and the fractional contributions of individual components are reported relative to this value. The uncertainties represent the central 68% confidence interval of the resampled synthetic photometry distributions. The uncertainties are generally less

[66] A full description can be found at http://www.astronomy.ohio-state.edu/MODS/Manuals/modsIDL.pdf.

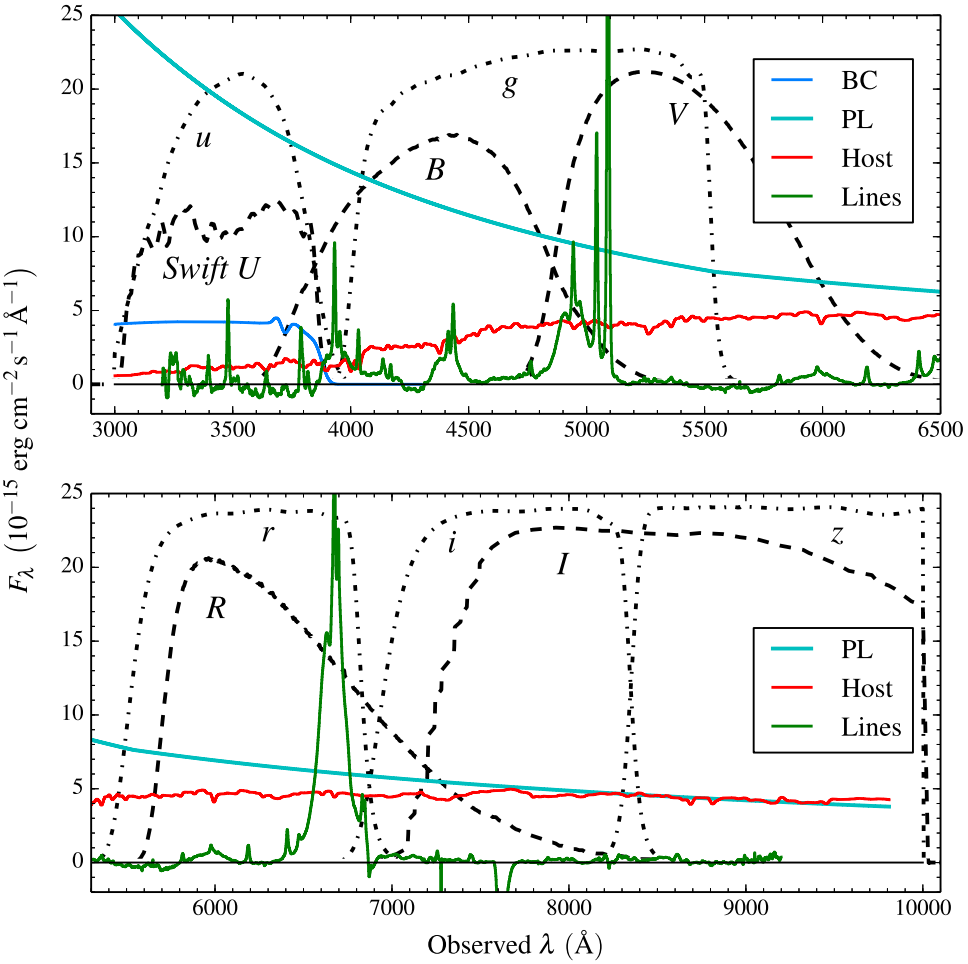

Figure 6. Decompositions of the MODS spectra from 2014 June 08, showing the contribution of the model components to different filters. "BC" is the Balmer continuum, "PL" is the power law, "Host" is the host-galaxy component, and "Lines" are the AGN emission lines. The emission lines are estimated by subtracting the total model from the observed spectrum. Johnson/Cousins optical filter transmission curves (and *Swift U*) are shown by the dashed black lines; SDSS filters are shown by the dot-dashed lines. The *Swift U* and *u* bands are truncated at 3000 Å and the *I* and *z* bands are truncated at 1 μm, in order to represent the atmospheric transmission cutoff.

than 1% because of the tight prior on the 5100 Å host-galaxy flux, which forces the galaxy template to be nearly constant and limits the variation of the other model components.

We do not consider effects of changing detector sensitivity with wavelength, since quantum efficiency curves for different instruments are usually much more variable than their filter transmission curves. Quantum efficiency will have the largest impact on the *I* and *z* filters, limiting the response of these filters at wavelengths shorter than the cutoff imposed at 1 μm. We investigated this effect by truncating the filter response at 9000 Å and repeating the experiment (essentially simulating a very steep quantum efficiency curve). We found that the final fractional contributions of the host/power-law components in these bands change by 1% or less and are therefore of minimal importance for our conclusions.

We find that the power-law component is dominant from the *u* band through the *V* band (>50% of the flux), although the host galaxy makes considerable contributions even in the *B* band (~20%). At longer wavelengths, the power-law component and host galaxy contribute roughly equal amounts of flux, except for the *r* and *R* bands, which include a substantial contribution from the Hα line: 20% in the *r* band and 15% in the *R* band. Line emission in all other filters is $\leqslant$10%. Balmer continuum emission accounts for about 19% of the flux in the *u* and *U* filters. The Mehdipour et al. (2015) blended Fe templates contribute <1% of the observed flux in the *g*, *V*, and *r* bands, confirming that Fe emission is a negligible component of the broadband fluxes of this object.

4.3. Impact on Time Delays

The final step is to estimate the impact of BLR emission on the recovered interband time delays. First, we simulate light curves for the AGN continuum, Balmer continuum, and BLR emission models. We then sum the component light curves to reproduce light curves as would be observed in a given filter, and we calculate the lag between the composite light curve and the *HST* 1367 Å continuum light curve.

The observed light curve is a superposition of the continuum emission and BLR emission,

$$X_{\rm obs}(t) = c(t) + l(t), \quad (5)$$

where $X_{\rm obs}$ is the observed light curve in filter *X*, $c(t)$ is the continuum light curve in that filter, and $l(t)$ is the line light

Table 8
Flux Percentage Contribution by Spectral Component

Filter	Total (10^{-11} erg cm^{-2} s^{-1})	PL (%)	BC (%)	Host (%)	Lines (%)
2014 June 08					
U	8.42	76.8 ± 1.5	16.7 ± 0.5	4.9 ± 0.1	2.3 ± 1.6
u	8.43	76.6 ± 1.5	16.7 ± 0.5	4.8 ± 0.1	2.7 ± 1.6
B	7.23	72.6 ± 0.9	1.4 ± 0.0	18.2 ± 0.5	7.6 ± 1.0
g	7.40	65.6 ± 0.6	⋯	24.3 ± 0.7	10.0 ± 0.8
V	7.39	59.0 ± 0.5	⋯	32.1 ± 0.9	9.1 ± 1.0
r	8.91	47.1 ± 0.4	⋯	33.4 ± 0.9	19.6 ± 1.0
R	8.44	48.9 ± 0.5	⋯	36.4 ± 1.0	14.8 ± 1.1
i	7.45	53.5 ± 0.7	⋯	48.5 ± 1.3	⋯
I	5.77	50.9 ± 0.7	⋯	50.3 ± 1.2	0.0 ± 0.1
z	4.60	49.5 ± 0.6	⋯	50.7 ± 1.0	0.0 ± 0.6
2014 June 25					
U	8.28	72.3 ± 1.5	21.4 ± 0.5	5.1 ± 0.1	1.0 ± 1.6
u	8.29	72.2 ± 1.5	21.4 ± 0.5	5.1 ± 0.1	0.6 ± 1.4
B	7.02	69.7 ± 1.0	1.8 ± 0.0	19.9 ± 0.2	8.5 ± 0.9
g	7.21	62.9 ± 0.7	⋯	26.6 ± 0.3	10.3 ± 0.9
V	7.29	55.9 ± 0.6	⋯	34.9 ± 0.4	9.0 ± 0.8
r	8.93	44.3 ± 0.4	⋯	35.8 ± 0.4	19.9 ± 0.7
R	8.47	46.0 ± 0.5	⋯	39.0 ± 0.4	15.0 ± 0.7
i	7.53	50.3 ± 0.6	⋯	51.9 ± 0.5	⋯
I	5.91	47.8 ± 0.5	⋯	53.7 ± 0.6	⋯
z	4.73	46.4 ± 0.5	⋯	54.0 ± 0.5	⋯
2014 June 08 (Blended Fe)					
U	8.49	82.6 ± 0.9	11.2 ± 0.5	5.3 ± 0.1	0.8 ± 1.1
u	8.49	82.4 ± 0.9	11.7 ± 0.5	5.3 ± 0.1	0.9 ± 1.1
B	7.23	73.5 ± 0.8	0.9 ± 0.0	20.0 ± 0.3	5.8 ± 1.0
g	7.40	64.5 ± 0.6	0.4 ± 0.0	26.7 ± 0.3	8.4 ± 0.8
V	7.38	55.9 ± 0.5	0.3 ± 0.0	35.3 ± 0.5	8.5 ± 0.7
r	8.90	44.2 ± 0.6	0.1 ± 0.0	36.6 ± 0.5	19.2 ± 0.6
R	8.43	45.7 ± 0.6	⋯	40.0 ± 0.5	14.4 ± 0.7
i	7.44	49.3 ± 0.9	⋯	53.3 ± 0.7	⋯
I	5.77	46.7 ± 0.9	⋯	55.0 ± 0.7	⋯
z	4.59	45.1 ± 0.9	⋯	55.4 ± 0.7	⋯
2014 June 25 (Blended Fe)					
U	8.41	82.8 ± 0.7	11.4 ± 0.4	5.8 ± 0.1	⋯
u	8.39	82.8 ± 0.7	12.0 ± 0.5	5.7 ± 0.1	⋯
B	7.02	70.7 ± 0.9	0.9 ± 0.0	22.8 ± 0.5	5.7 ± 1.2
g	7.21	60.7 ± 0.8	0.4 ± 0.0	30.5 ± 0.7	8.5 ± 1.3
V	7.27	50.4 ± 0.8	0.3 ± 0.0	40.1 ± 0.9	9.4 ± 1.2
r	8.88	38.4 ± 0.7	0.1 ± 0.0	41.3 ± 0.9	20.4 ± 1.1
R	8.40	39.6 ± 0.8	⋯	45.2 ± 1.0	15.5 ± 1.2
i	7.46	41.9 ± 0.8	⋯	60.3 ± 1.3	⋯
I	5.82	38.9 ± 0.9	⋯	62.5 ± 1.1	⋯
z	4.65	37.2 ± 0.9	⋯	63.2 ± 0.9	0.0 ± 0.1

Note. PL is power law, BC is Balmer continuum, host is the host galaxy, lines are AGN emission lines. BC includes an Fe emission template in the "Blended Fe" models.

curve, assumed to originate in the BLR. We use the term "line light curve" to refer to any emission produced in the BLR, including the Balmer continuum.

To simulate $c(t)$, we calculated the lag $\tau_{\rm cont}$ implied by the best-fit parameters in Figure 5 ($\alpha = 0.79 \pm 0.22$ and $\beta = 0.99 \pm 0.14$ in Equation (4)) at the pivot wavelength of the filter, and we shifted the JAVELIN DRW model of the *HST* 1367 Å light curve by this amount. This method assumes that the *HST* 1367 Å light curve drives $c(t)$ through instantaneous reprocessing after some light-travel-time delay, as would be expected for X-ray reprocessing in the accretion disk.[67]

[67] Reprocessed emission is also expected to be somewhat smoothed in time compared to the driving light curve. We therefore also considered versions of $c(t)$ that are both smoothed and shifted by convolving the JAVELIN 1367 Å model with a top-hat function of amplitude $1/(2\tau_{\rm cont})$ for $0 < \tau < 2\tau_{\rm cont}$. We found that this smoothing made very little difference on the results, and so we only discuss the results for the shifted versions of $c(t)$ here.

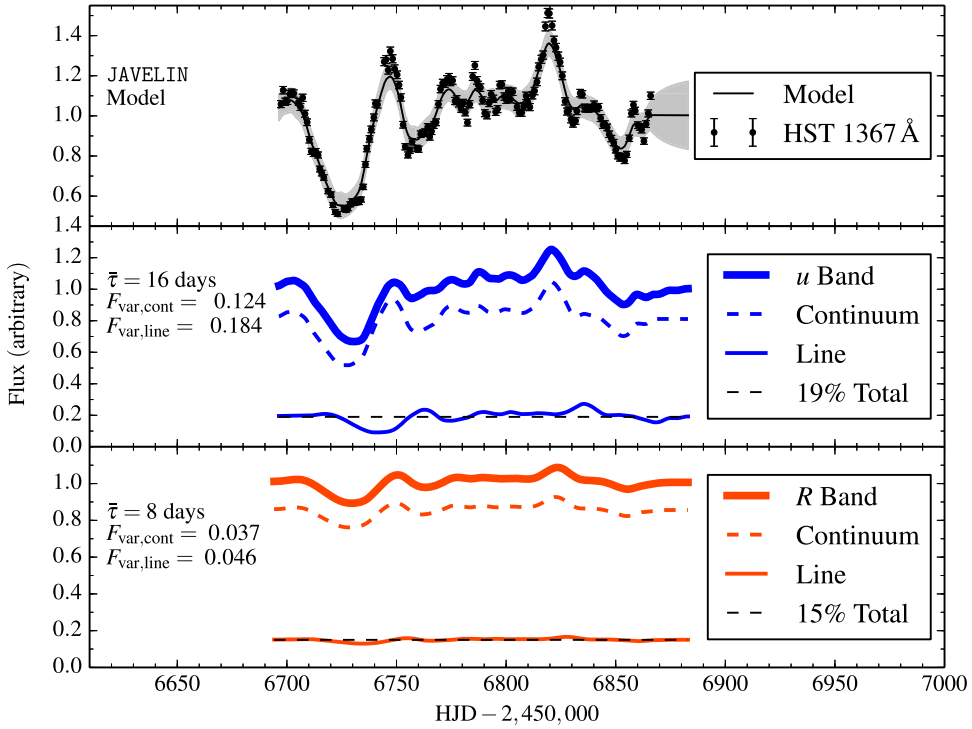

Figure 7. Examples of mock light curves, $c(t)$, $l(t)$, and $X_{\rm obs} = c(t) + l(t)$, used for the analysis in Section 4.3. The top panel shows the *HST* 1367 Å light curve and the JAVELIN model used to generate the mock light curves, with the 1σ uncertainty shown by the gray band. The middle panel displays an example of a mock *u*-band light curve, with a large line lag and high fractional variability, likely to result in the largest change of the observed lag. The bottom panel shows an example of a mock *R*-band light curve, with a more realistic line lag and fractional variability, chosen to be consistent with the Hβ light curve. See Section 4.3 for further details.

In RM, the line emission is assumed to be powered by ionizing continuum emission, so that

$$l(t) = \int \Psi(\tau) C(t - \tau) d\tau, \tag{6}$$

where $C(t)$ is the driving continuum light curve and $\Psi(\tau)$ is the transfer function. For simplicity, we assume $C(t)$ equal to the JAVELIN model of the *HST* 1367 Å light curve and a top-hat transfer function,

$$\Psi(\tau) = \frac{1}{w} \text{ for } (\bar{\tau} - w/2) < \tau < (\bar{\tau} + w/2), \tag{7}$$

where $\bar{\tau}$ is the mean line lag and w is the width of the smoothing kernel. The choice of a top-hat function is for mathematical convenience and does not reflect any particular geometry, although it is widely consistent with a range of BLR configurations (for example, a spherical shell or the gross properties of an inclined disk/annulus; Peterson 2001). We varied $\bar{\tau}$ and w by octaves, with $\bar{\tau} = 2$, 4, 8, and 16 days and $w = 0$, 2, 4, 8, and 16 days. These values were chosen to sample the parameter space near the mean Hβ lag during the monitoring campaign (8.57 ± 0.67 days; Paper V). To a low approximation, the Balmer continuum and Hα lag would be expected to lie near this value. Finally, we enforced causality by setting $\Psi(\tau) = 0$ for $\tau < 0$.

We simulate light curves for the *u, U, r*, and *R* bands, in order to investigate the impact of Balmer continuum and Hα emission on the recovered lags. After generating the grid of shifted and smoothed line light curves, we renormalized each so as to reproduce the level of BLR contamination inferred from the spectral decomposition (Table 8). We then adjusted the fractional variability amplitude $F_{\rm var}$ (defined in Section 2.4) of both the continuum and line light curves to match their observed values. For the continuum light curves, $F_{\rm var,cont}$ is estimated directly from the observed broadband light curves (Table 5, column (9)). For the line light curves, we set $F_{\rm var,line} = 4.6\%$, derived from the observed Hβ light curve (Paper V). We also experimented with changing the fractional variability amplitude of the line light curve to $F_{\rm var,line} = 0.012$, 0.023, 0.092, and 0.184. Examples of two composite light curves and their model components, $c(t)$ and $l(t)$, are shown in Figure 7.

After constructing $c(t)$ and $l(t)$ for each model, we calculated the lags of these light curves relative to $C(t)$ using the ICCF method described in Section 3. In all cases, we recovered the input values of $\bar{\tau}$ and $\tau_{\rm cont}$ to within the time resolution of the model light curves (0.12 days). We then calculated the ICCF for the composite light curve $c(t) + l(t)$, finding that the recovered lags are most sensitive to the choice of $F_{\rm var,line}$ and $\bar{\tau}$ but are virtually independent of w. The resulting mean lags are shown in Figure 8 as a function of input $\bar{\tau}$ for the three values of $F_{\rm var,line}$ near that of Hβ (larger or smaller values of $F_{\rm var,line}$ do not plausibly reproduce the observed lags and are omitted for clarity). Larger values of these parameters tend to increase the recovered lag, but at the fiducial values of Hβ the change is 0.6–1.2 days (blue point in Figure 8 with $\bar{\tau} = 8$).

We also checked for an effect of BLR contamination on the lag uncertainties. For each model, we found that larger values of $F_{\rm var,line}$ and $\bar{\tau}$ tend to increase the width of the ICCF. However, there was no correlation between these parameters and the location or width of the ICCF centroid distribution. This means that the lag uncertainties depend more sensitively

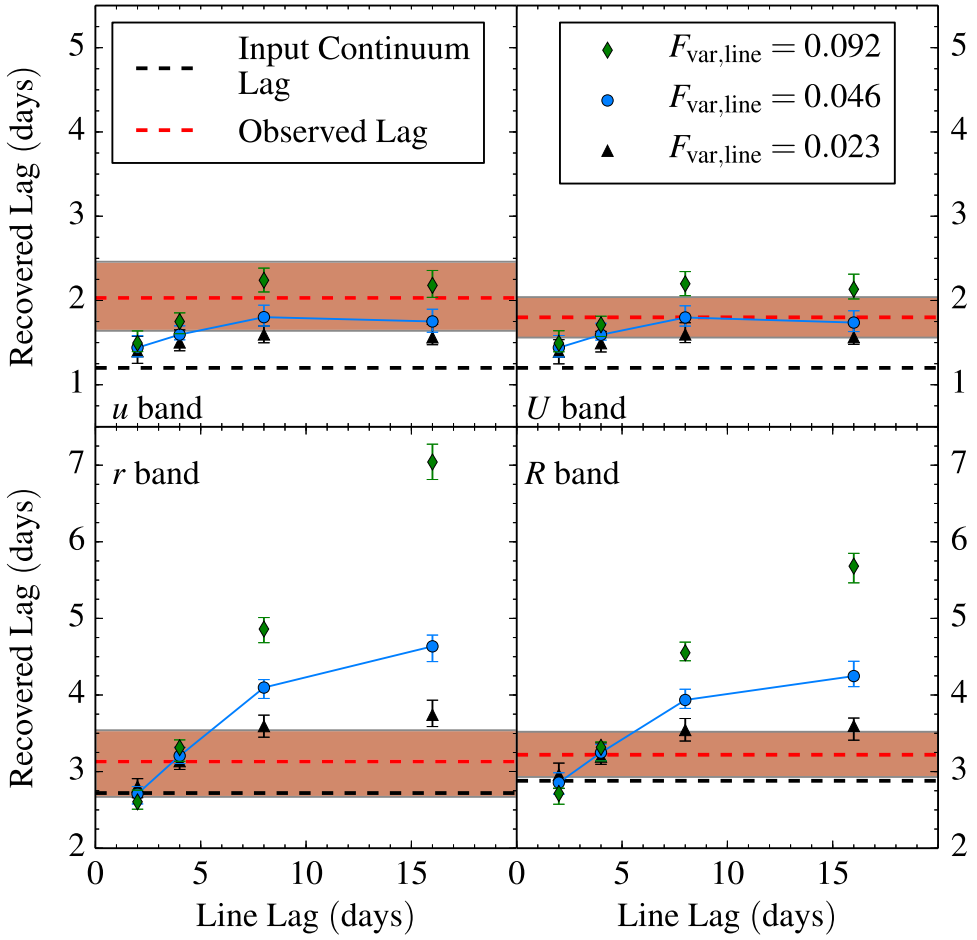

Figure 8. Recovered lags of mock light curves as a function of input line light curve $l(t)$ lag. The colored points show the results for different variability amplitudes of the line light curve. The solid blue lines indicate the variability amplitude observed in the Hβ light curve. The black dashed line represents the input lag of the continuum light curve $c(t)$, while the red dashed line is the observed lag and the red band is its 1σ uncertainty. See Section 4.3 for further details.

on the light curve quality rather than on any BLR contamination.

For values of $F_{\rm var,line}$ that are smaller than $F_{\rm var,cont}$ ($F_{\rm var,line} \leqslant 0.023$ in r and R and $\leqslant 0.092$ in u and U), the input line lag only has a limited effect on the recovered lag, evidenced by the flattening of the trends in Figure 8. This result is in contrast to the simple expectation that the observed lag is the flux-weighted mean lag of the line and continuum light curves, which scales linearly with the line lag. Instead, it appears that the observed lag only follows the line lag if the BLR emission dominates the variability properties of the composite light curve, as seen for the mock r and R bands at large $F_{\rm var,line}$. This indicates that the bias of the continuum lag introduced by BLR emission will usually be limited for broadband filter light curves that are dominated by continuum emission, although the bias may still be important for small continuum lags.

Our simulations with these fiducial Hβ parameters produce u- and U-band lags in excellent agreement with the observed lags, while the simulated r- and R-band lags overestimate the observed lag by about 1 day. Our current campaign cannot directly address the issue of the unknown values of $F_{\rm var,line}$ and $\bar{\tau}$ for these reverberations. However, it is expected from photoionization modeling that the Balmer continuum has a larger response ($F_{\rm var,line}$) but shorter lag than Hβ, while Hα should have a smaller response but longer lag (Korista & Goad 2001, 2004). Based on Figure 8, this would serve to reduce the discrepancy between the recovered and observed lag in the r and R bands, while the recovered and observed lag in the u and U bands would remain in good agreement.

Thus, our simulations suggest that contamination by BLR emission can reasonably account for the systematic offset of the measured u, U, r, and R lags above the fit in Figure 5. This bias is well resolved in the u and U bands (the offset from the fit in Figure 5 is 2.0σ and 2.5σ, respectively), but of small importance in the r and R bands (0.6σ and 1.7σ, respectively). This result justifies our exclusion of the u- and U-band data in the fit to Equation (4).

Chelouche & Zucker (2013) and Chelouche (2013) claim that BLR emission is responsible for the large $B-R$/Cousins I lags in the Sergeev et al. (2005) NGC 5548 light curves, and they find optical continuum lags consistent with 0 days. This is at odds with our results, since the BLR biases would have to be $\gtrsim$8 days. These studies use a variation of the ICCF method (the multivariate CCF) to disentangle line and continuum lags from emission observed in a single filter. As we have already noted, gaps in the Sergeev et al. (2005) data make cross-correlation functions that rely on interpolation unreliable. Furthermore, this bias would imply that line emission contributes 30%–50% of the flux in the R and Cousins I bands, which is implausibly high based on both our spectral decompositions and the composite Seyfert 1 spectrum of Chelouche (2013).

5. DISCUSSION

5.1. UV/Optical Light Curves and Lags

A primary goal of the AGN STORM project was to investigate how the continuum emission changes as a function of wavelength and to assess any systematic issues introduced by using the optical continuum in place of the far-UV or extreme-UV. Figure 2 shows a detailed comparison of the *HST* 1367 Å light curve and all other data used in this study. We draw particular attention to the ground-based *V*-band light curve, since this is the most common choice of ionizing continuum proxy in ground-based RM studies. All of the major events and salient characteristics of the 1367 Å light curve are reproduced in the *V* band. There are, however, several noticeable differences.

5.1.1. UV–Optical Lags

The first difference is a time delay between variations in the UV and optical light curves. Emission at 1158 Å, the shortest continuum wavelength available in this study, probably originates from a region of the accretion disk similar to that of the true ionizing continuum at $\lambda \leqslant 912$ Å. This is because the lag–wavelength relation must flatten at small wavelengths (owing to the inner edge of the disk), but the inner edge already makes an important contribution to emission at ∼1000 Å (Novikov & Thorne 1973, pp. 343–450). Extrapolating the fit from Equation (4) to $\lambda = 912$ Å implies a 0.26-day lag relative to the 1367 Å light curve, which is in reasonable agreement with the 1367–1148 Å lag (-0.16 ± 0.16 days). We therefore adopt a value of 0.2 days for the lag between the true ionizing continuum and the 1367 Å emission, since the lags for wavelengths <912 Å are unlikely to be much larger. This translates to a distance between the true ionizing continuum and the optically emitting portion of the disk of ∼2.2 lt-day. A consequence of this UV–optical lag is that the radius of the BLR in NGC 5548 is underestimated when derived from the optical–Hβ lag. The optical–Hβ lag is variable in time but typically has a value between 6 and 20 days (Peterson et al. 2004; Zu et al. 2011). Thus, if a similar UV–optical lag exists in other AGNs, the physical size of the BLR is being systematically underestimated by up to ~37% (or 11% for a lag of 20 days).

This result does not affect current optical RM SMBH masses, because RM only directly measures the virial product of the BLR, $c\tau(\Delta V)^2/G$, where τ is the BLR lag and ΔV^2 is its velocity dispersion (estimated from line-profile widths). Since the geometry and dynamics of the BLR are unknown, the virial product must be rescaled by a factor f in order to produce an SMBH mass. While every AGN has a different value of f, a statistical average $\langle f \rangle$ can be calculated by calibrating an ensemble of virial products to some other SMBH mass estimate. Currently, this is done using the M–σ relation of local quiescent galaxies (Onken et al. 2004; Woo et al. 2010, 2013, 2015; Park et al. 2012a, 2012b; Grier et al. 2013a). Thus, any systematic misestimation or bias of the lag (or velocity dispersion) is compensated by the calibration of $\langle f \rangle$, while the uncertainty of a single RM SMBH mass is dominated by the statistical uncertainty in $\langle f \rangle$, currently about 25%–33% (Grier et al. 2013a; Woo et al. 2015). However, any physical interpretation of $\langle f \rangle$ (for example, a measure of the mean inclination of the BLR, assuming a disk or otherwise flattened geometry) requires a recalibrated value of $\langle f \rangle$ that takes into account the UV–optical lag.

Single-epoch SMBH mass estimates are also unaffected by this result, since the radius–luminosity (RL) relation is inferred from a sample of RM AGNs. While the larger BLR radius measured from the UV data would increase the normalization of the RL relation, a recalibration of $\langle f \rangle$ exactly cancels this change. The UV–optical lag may introduce a second-order effect on single-epoch SMBH masses, if it is found that the magnitude of the UV–optical lag correlates with continuum luminosity or SMBH mass. Furthermore, the magnitude of the lag depends on accretion rate (see Section 5.3), which may also add scatter to existing mass–scaling relations. To investigate these effects, more simultaneous UV and optical RM experiments must be executed, using a sample of AGNs with a wide range of luminosities.

Finally, the UV–optical lag has an impact on masses derived from direct dynamical modeling of RM data, since this method interprets the continuum-line lag as a measure of the physical radius of the BLR. To a low approximation, a larger BLR radius implies a proportionally larger SMBH mass. The effect of using UV continuum light curves for dynamical modeling studies will be investigated in future papers in this series, but until such modeling is complete, we adopt an RM-based SMBH mass for NGC 5548, since this estimate is less model dependent. From the Hβ virial products compiled by Bentz & Katz (2015), and taking $\langle f \rangle = 4.3 \pm 1.1$ (Grier et al. 2013b), we adopt a mass of $(5.2 \pm 1.3) \times 10^7\, M_\odot$ for the SMBH in NGC 5548. We note that this value moves in the correct direction for a larger BLR but is still consistent within the quoted uncertainties of the dynamically modeled mass in Pancoast et al. (2014).

5.1.2. Optical Smoothing

The second difference between the UV and optical continuum light curves is that the *V*-band light curve appears to be smoother than the *HST* light curve. For example, the rapid oscillations in the UV light curve between HJD = 2,456,760 and 2,456,810 also appear in the *V*-band light curve, but at a much smaller amplitude with gentler inflections. The smoothing becomes increasingly severe at longer wavelengths where the amplitude of short-timescale variations decreases (see Section 2.4). These effects were also seen in NGC 2617 by Shappee et al. (2014), NGC 6814 by Troyer et al. (2016), and MCG-6-30-15 by Lira et al. (2015). Increased smoothing and decreased amplitudes are expected if shorter-wavelength emission drives the optical continuum, since the size, structure, and inclination of the accretion disk define a "continuum transfer function" that smooths the reprocessed light curve, while geometric dilution decreases the energy flux incident on large disk radii that contribute most to longer-wavelength emission.

In practical terms, the sharpest and strongest features in the *V*-band AGN STORM light curve are only slightly affected by this smoothing. Since these features provide the most leverage for constraining the CCF (Peterson 1993), we conclude that the smoothing of the optical continuum is not important for ground-based RM studies that aim only to recover a mean emission-line lag and an SMBH mass. The smoothing may be more problematic for reconstructing velocity-delay maps, direct dynamical modeling, or regularized linear inversion (Horne et al. 1991, 2004; Bentz et al. 2010a; Grier et al. 2013b;

Pancoast et al. 2014; Skielboe et al. 2015). These methods are very sensitive to the fine structure of the driving continuum light curve, and smoothing the light curve will erase information that would otherwise be helpful for reconstruction of the geometry and dynamics of the BLR. Velocity-delay maps, dynamical modeling, and regularized linear inversion for this data set will be presented in upcoming papers in this series.

5.1.3. Magnitude of UV–Optical Lags

The large lags measured for optical bands, shown in Figure 5, are comparable to, and sometimes larger than, the lags for high-ionization-state lines such as He II λ1640 and C IV λ1549 (Paper I). If the lags do in fact represent light-travel times across the accretion disk, then the optically emitting portion of the accretion disk appears to have a similar physical extent to the highly ionized portion of the BLR. This situation implies a close connection between the BLR and continuum-emitting source. For example, BLR clouds may be directly above or interior to the portion of the accretion disk emitting in the optical. Another plausible hypothesis is that at least part of the inner, high-ionization BLR emission arises from a wind launched from the surface of the accretion disk (e.g., Collin-Souffrin 1987; Chiang & Murray 1996; Proga & Kurosawa 2010). Such models are able to reasonably explain many observed features of AGN emission lines, including their profiles, variability, and absorption characteristics (see Proga & Kallman 2004; Eracleous et al. 2009; Denney 2012; Higginbottom et al. 2014, and references therein). Alternatively, the accretion disk may smoothly merge with the BLR somewhere near 2–3 lt-day (for an analysis of this family of models, see, e.g., Goad et al. 2012). Future papers in this series will attempt to map the geometry and kinematics of the inner BLR using the reverberation signal of high-ionization-state lines, which may shed further light on the connection between the accretion disk and BLR.

5.2. BLR Emission and Broadband Filter Lags

Based on our spectral decomposition, approximately 19% of the observed emission in the *u* and *U* bands is Balmer continuum emission from the BLR, while 15%–20% of *r*- and *R*-band emission is the prominent Hα line. These ratios may change with time, as shown in Table 8, depending on the luminosity state of the AGN, the difference in phase between the continuum and line light curves, and the light curves' variability amplitudes. For mean flux levels near the BLR contamination in the *u, U, r*, and *R* bands, as well as variability amplitudes and line lags that match the observed Hβ light curve, our experiments with mock light curves indicate biases in the interband continuum lag of ~0.6–1.2 days.

These results depend on the assumption that all BLR emission light curves have properties similar to the Hβ light curve. It is likely that the diffuse continuum actually has a stronger response but smaller lag than Hβ, while Hα is expected to have a weaker response but larger lag (Korista & Goad 2001, 2004; Bentz et al. 2010b). Since these parameters have offsetting effects, it is unlikely that the lag biases caused by BLR contamination are larger than the fiducial estimates presented here (see Figure 8). Future RM programs can test this result by specifically targeting the diffuse continuum and Hα emission, putting stronger constraints on their variability amplitudes and mean lags.

The systematic tendency for the *u-, U-, r-*, and *R*-band lags to sit above the fit in Figure 5 can therefore reasonably be explained by BLR contamination. In the case of the *u* and *U* bands, the offset from the fit to Equation (4) is large compared to the predicted lag (as well as the observational uncertainty), which supports our decision to exclude these data from the final model. On the other hand, the *r*- and *R*-band offsets are much smaller, so the BLR bias probably makes little difference for our final model. Extending this reasoning to the *B*-, *g*-, and *V*-band filters, the BLR contamination is less than 10%, which would result in even smaller biases.

It is therefore unlikely that there are any important biases of the continuum lags in these bands, unless the diffuse continuum component (e.g., free–free emission or the Paschen continuum) makes a substantial contribution. This diffuse continuum component of the spectrum is unconstrained in our spectral decomposition, but it provides an intriguing possibility of explaining the downturn of the lag–wavelength relation in the *I* and *z* bands. The Paschen continuum begins at 8204 Å, between the *i* and *I* bands, so the true continuum lag–wavelength relation may run through the UV and *Iz*-band lags, but underneath the lags of the other optical filters. The viability of this explanation requires significant contamination of the optical filters by diffuse BLR emission, which can potentially be estimated through photoionization modeling of the *HST* data or additional optical/near-IR observations.

5.3. Accretion-disk Size

A geometrically thin, optically thick, irradiated accretion disk makes definite predictions about the observed lag–wavelength structure of the AGN. Here we compare this model to the observed continuum lags, although we do not necessarily interpret the model parameters as indicative of physical conditions within the AGN. Full physical modeling of the AGN STORM data is deferred to future papers in this series (C. S. Kochanek et al. 2016, in preparation; D. A. Starkey et al. 2016, in preparation).

The disk is assumed to have a fixed aspect ratio with scale height much smaller than radius and is heated internally by viscous dissipation and externally by a UV/X-ray source near the SMBH at a small height *H* above the disk. In such a scenario, the temperature profile is

$$T(R) = \left(\frac{3GM\dot{M}}{8\pi\sigma R^3} + \frac{(1-A)L_X H}{4\pi\sigma R^3} \right)^{1/4}, \quad (8)$$

where *M* is the mass of the central SMBH, $\dot{M}$ is the mass accretion rate of the disk, *R* is the distance away from the black hole and central source of heating radiation, L_X is the luminosity of the heating radiation, and *A* is the albedo of the disk (Cackett et al. 2007). Here we have ignored the inclination and the inner edge of the disk, as well as any relativistic effects. Inclination and relativity may have a small impact on the temperature profile, but the largest effect is caused by the inner edge, which reaches a maximum temperature and probably makes important contributions to emission at wavelengths <2000 Å (Novikov & Thorne 1973). This introduces an error when comparing the *HST* lags to this model, although the effect is small relative to the UV–optical lags.

Identifying the temperature with a characteristic emission wavelength $T = Xhc/k\lambda$, where *X* is a multiplicative factor of

order unity, and the radius with the light-travel time $R = c\tau$, we have

$$c\tau = \left(X\frac{k\lambda}{hc}\right)^{4/3}\left(\frac{3GM\dot{M}}{8\pi\sigma} + \frac{(1-A)L_{\rm X}H}{4\pi\sigma}\right)^{1/3}. \quad (9)$$

The factor X accounts for systematic issues in the conversion of T to λ for a given R, since a range of radii contributes to emission at λ. From the flux-weighted mean radius

$$\langle R\rangle = \frac{\int_{R_0}^{\infty} B(T(R))R^2\,dR}{\int_{R_0}^{\infty} B(T(R))R\,dR}, \quad (10)$$

we derive $X = 2.49$, where R_0 is the inner edge of the disk, $B(T(R))$ is the Planck function, and $T(R)$ is the temperature profile defined in Equation (8).[68]

If we measure τ relative to a reference time delay τ_0 of a light curve with effective wavelength λ_0, then this becomes

$$(\tau-\tau_0) = \frac{1}{c}\left(X\frac{k\lambda_0}{hc}\right)^{4/3}\left(\frac{3GM\dot{M}}{8\pi\sigma} + \frac{(1-A)L_{\rm X}H}{4\pi\sigma}\right)^{1/3} \times\left[\left(\frac{\lambda}{\lambda_0}\right)^{4/3} - 1\right]. \quad (11)$$

Therefore, the parameter α in Equation (4) is related to the energy generation rate responsible for heating the disk, while β is predicted to be $4/3$. The absolute size of the disk at λ_0 can be measured by determining τ_0, which is inferred by assuming that the corona is located at $\tau = 0$ and fitting the X-rays lags (in which case $\tau_0 = \alpha$).

We can only determine $\dot{M}$ indirectly through an estimate of the bolometric luminosity. We set $L_{\rm Bol} = \eta\dot{M}c^2$, where η is the radiative efficiency for converting rest mass into radiation, and $L_{\rm Bol}$ quantifies all emergent radiation from the AGN, including coronal X-rays (in this sense, our model differs from the typical Shakura & Sunyaev [1973] thin-disk model). A convenient parameterization of $L_{\rm Bol}$ is the Eddington ratio, $\dot{m}_{\rm E} = L_{\rm Bol}/L_{\rm Edd}$. We also simplify Equation (11) by taking $(1-A)L_{\rm X}H/R = \kappa GM\dot{M}/2R$, where κ is the local ratio of external to internal heating, assumed to be constant with radius.

The equation for α is then

$$\alpha = \frac{1}{c}\left(X\frac{k\lambda_0}{hc}\right)^{4/3}\left[\left(\frac{GM}{8\pi\sigma}\right)\left(\frac{L_{\rm Edd}}{\eta c^2}\right)(3+\kappa)\dot{m}_{\rm E}\right]^{1/3}. \quad (12)$$

A common choice for $\dot{m}_{\rm E}$ is 0.1, and we further assume that $\eta = 0.1$ and $\kappa = 1$ for our fiducial calculations (i.e., the X-rays and viscous heating contribute equal amounts of energy to the disk). For a $5.2\times10^7 M_\odot$ SMBH, these assumptions give $\alpha = 0.14$ days. If we increase the accretion rate by setting $\dot{m}_{\rm E} = 1$ and 10, then $\alpha = 0.29$ and 0.63 days, respectively. The lag–wavelength relation for these models is shown in Figure 5, and the curves for $\dot{m}_{\rm E} = 1$–10 bracket our fit to Equation (4) with $\alpha = 0.79\pm0.22$ days and $\beta = 0.99\pm0.14$. However, it is important to note that the disk probably does not remain geometrically thin at these high accretion rates, and the assumptions of the model do not hold in this regime (Jiang et al. 2014; Sądowski et al. 2014). Equation (12) is relatively insensitive to the ratio of external to internal heating—even if the X-rays contribute a negligible portion of the luminosity ($\kappa = 0$), α would only change by a factor of $(3/4)^{1/3}$.

[68] Alternative definitions of R exist. For example, a weighting function that better characterizes the radius responding to variable irradiation would replace Equation (8) with $T = T_0(R) + \partial B(T(R))/\partial T\frac{\delta T}{T}T$ and set $(\delta T/T)$ equal to a constant fractional temperature variation. This yields $X = 3.37$.

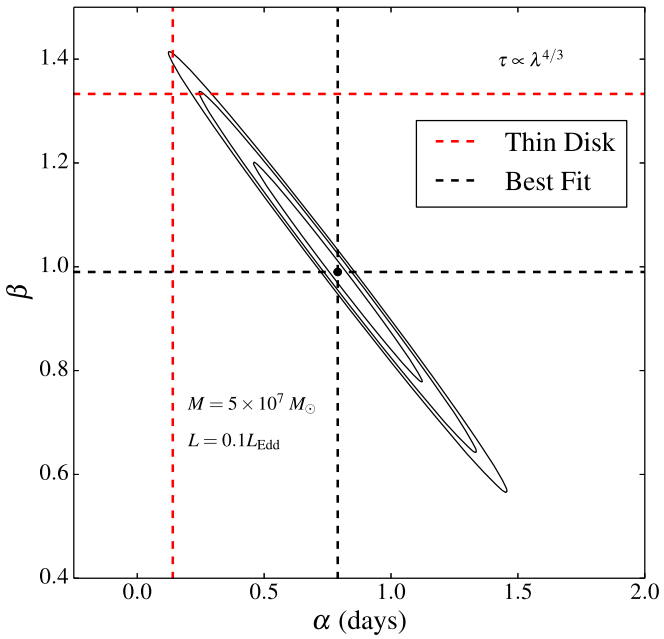

Figure 9. Probability distribution for the parameters α and β of our best-fit model. The contours show the 68%, 95%, and 99% confidence regions.

In Paper II, we found $\alpha = 0.35\pm0.04$ days, somewhat smaller than in this study. The smaller value can be explained by correlations between α and β, shown in Figure 9. For the final analysis in Paper II, β was fixed to $4/3$, and if we do the same, we find $\alpha = 0.42\pm0.02$ days, in good agreement with Paper II. The fit with fixed β has $\chi^2/{\rm dof} = 1.42$, making the lower value of $\beta = 0.99\pm0.14$ statistically preferred. However, this result is driven by the flattening of the lags at the reddest wavelengths. If we exclude the I and z bands from the fit (as well as u and U), we find $\beta = 1.18\pm0.19$ and $\alpha = 0.58\pm0.20$ days with $\chi^2/{\rm dof} = 0.89$, while fixing $\beta = 4/3$ gives $\alpha = 0.45\pm0.02$ days and $\chi^2/{\rm dof} = 0.87$.

We therefore conclude that a reprocessing model can fit the data reasonably well but requires a much larger disk radius than predicted by standard thin-disk models. Fixing $\beta = 4/3$ (in order to match the theoretical temperature profile), our best-fit value of $\alpha = 0.42$ days is a factor of 3.0 larger than the standard prediction with $L/L_{\rm Edd} = 0.1$.

A sufficiently high accretion rate can account for this difference by increasing the size of the accretion disk. We note that uncertainties in the SMBH mass do not require $\dot{m}_{\rm E}$ to be larger than 1, since $\dot{m}_{\rm E}\propto\alpha^3/M^2$ (Equation (12)), while the SMBH mass may be up to 1.75 times larger at 3σ than our adopted value. This would still require $\dot{m}_{\rm E}$ to be somewhere in the range of ~0.1–1. On the other hand, a comparison of $\dot{m}_{\rm E}$ can be made assuming a thin-disk spectrum and using the observed optical luminosity (e.g., Collin et al. 2002; Netzer 2013, Equation (4.53)). From our spectral decompositions, we estimate that $\lambda F_\lambda = 4.57\times10^{-11}\,{\rm erg\,cm^{-2}\,s^{-1}}$ at 5100 Å, which yields $\dot{m}_{\rm E} = 0.05$ at a disk inclination of $\cos i = 0.63$

and radiative efficiency $\eta = 0.1$. The accretion rate cannot be much higher (unless the disk is seen very edge-on), so this result implies that a standard thin-disk model cannot account for both the observed time delays and the monochromatic luminosity at 5100 Å.

The large disk size found here corroborates the results from Paper II and other recent RM studies (McHardy et al. 2014; Shappee et al. 2014; Lira et al. 2015). The measurements of large disk radii are also in good agreement with the sizes inferred from gravitational microlensing experiments (see Figure 6 in Paper II, as well as Poindexter et al. 2008; Morgan et al. 2010; Mosquera et al. 2013). Other sources of tension with the thin-disk/continuum reprocessing model are (1) the weak correlation between the X-ray light curves and UV/optical light curves (Paper II) and (2) the possible flattening of the lags at the longest wavelengths. The latter phenomenon might contain information about the outer edge of the disk, or perhaps be explained by contaminating emission from BLR material along the line of sight (Korista & Goad 2001), and/or emission from the inner edge of the near side of the obscuring torus (Goad et al. 2012).

The intriguing result that accretion disks in AGNs might be larger than predicted by standard thin-disk theory depends on only a handful of lensed quasars and three RM AGNs (NGC 5548, NGC 2617, and MCG-6-30-15; Shappee et al. 2014; Lira et al. 2015). Thus, it is important to carry out further continuum RM experiments, in order to establish whether this is a robust result and determine what physical parameters govern the disk size. It is also possible to recast this kind of experiment in more direct scaling relations, such as the lag–luminosity relations of Sergeev et al. (2005), which can be derived from thin-disk theory (both the disk size and luminosity scale with accretion rate and black hole mass). In fact, the Sergeev et al. (2005) lag–luminosity relations lie somewhat above the prediction for standard thin-disk theory, and the lags reported here would be ∼1 day below these relations in most bands. However, the relations are largely based on unresolved lags and have very large uncertainties, so they do not put an interesting constraint on model predictions. A larger sample of AGNs with continuum lags derived to the same precision as this study would provide an interesting measurement of the lag–luminosity relations, which can provide a further test of thin-disk theory and establish whether larger disk sizes are generic properties of the AGN population.

6. SUMMARY

We have presented results for a ground-based, broadband photometric monitoring campaign of NGC 5548. Our light curves are of very high quality, achieving cadences of $\lesssim$1 day in nine optical bands over an entire observing season. Using full optical-wavelength spectra and synthetic photometry, we estimated the relative contribution of host-galaxy starlight, AGN continuum emission, Balmer continuum, and line emission from the BLR to the observed light curves. Our main results are as follows.

(1) Significant time delays are detected between the far-UV, near-UV, and optical broadband light curves. The delay between emission at 1367 and 2600 Å is less than 1 day, and the delay between emission at 1367 Å and the V band is about 2 days. Such large time delays are comparable to, and sometimes greater than, the lags of the high-ionization-state emission lines, suggesting that the continuum-emitting source is of a physical size approximately equal to the inner BLR.

(2) If similar interband continuum lags exist in other AGNs, this also suggests that the size of the BLR is 11%–37% larger than would be inferred from optical data alone. However, there do not appear to be other significant systematic effects associated with the optical light curves, and RM SMBH masses are not affected by this result.

(3) There is some contamination of the broadband light curves by BLR emission, with 19% of the u and U bands attributable to the Balmer continuum, and 15%–20% of the r and R bands attributable to Hα. The impact of BLR emission on the observed u- and U-band lags is ∼0.6–1.2 days, but it is probably unimportant in the r and R bands. This justifies our decision to exclude the u- and U-band lags from our final analysis.

(4) The trend of lag with wavelength is broadly consistent with the prediction for continuum reprocessing by a geometrically thin accretion disk with $\tau \propto \lambda^{4/3}$. However, the size of the disk is a factor of 3 larger than the prediction for standard thin-disk theory, assuming that $L = 0.1\,L_{\rm Edd}$. This result appears to corroborate those from other continuum RM projects and gravitational microlensing studies. Further investigations of the accretion-disk structure will benefit from physical modeling of the AGN STORM light curves, and several such studies are planned for upcoming papers in this series (C. S. Kochanek et al. 2016, in preparation; D. A. Starkey et al. 2016, in preparation).

The LBT is an international collaboration among institutions in the United States, Italy, and Germany. LBT Corporation partners are The Ohio State University, and The Research Corporation, on behalf of The University of Notre Dame, University of Minnesota, and University of Virginia; The University of Arizona on behalf of the Arizona university system; Istituto Nazionale di Astrofisica, Italy; and LBT Beteiligungsgesellschaft, Germany, representing the Max-Planck Society, the Astrophysical Institute Potsdam, and Heidelberg University.

This paper used data obtained with the MODS spectrographs built with funding from National Science Foundation (NSF) grant AST-9987045 and the NSF Telescope System Instrumentation Program (TSIP), with additional funds from the Ohio Board of Regents and the Ohio State University Office of Research. This paper made use of the `modsIDL` spectral data reduction pipeline developed in part with funds provided by NSF Grant AST—1108693.

The Liverpool Telescope is operated on the island of La Palma by Liverpool John Moores University in the Spanish Observatorio del Roque de los Muchachos of the Instituto de Astrofisica de Canarias with financial support from the UK Science and Technology Facilities Council.

KAIT and its ongoing operation were made possible by donations from Sun Microsystems, Inc., the Hewlett-Packard Company, AutoScope Corporation, Lick Observatory, the NSF, the University of California, the Sylvia and Jim Katzman Foundation, and the TABASGO Foundation. Research at Lick Observatory is partially supported by a generous gift from Google.

Support for *HST* program number GO-13330 was provided by NASA through a grant from the Space Telescope Science Institute, which is operated by the Association of Universities for Research in Astronomy, Inc., under NASA contract NAS5-26555. M.M.F., G.D.R., B.M.P., C.J.G., and R.W.P. are grateful for the support of the NSF through grant AST-1008882 to The Ohio State University. A.J.B. and L.P. have been supported by NSF grant AST-1412693. A.V.F. and W.-K.Z. are grateful for financial assistance from NSF grant AST-1211916, the TABASGO Foundation, and the Christopher R. Redlich Fund. M.C. Bentz gratefully acknowledges support through NSF CAREER grant AST-1253702 to Georgia State University. M.C. Bottorff acknowledges HHMI for support through an undergraduate science education grant to Southwestern University. K.D.D. is supported by an NSF Fellowship awarded under grant AST-1302093. R.E. gratefully acknowledges support from NASA under awards NNX13AC26G, NNX13AC63G, and NNX13AE99G. J.M.G. gratefully acknowledges support from NASA under award NNH13CH61C. P.B.H. is supported by NSERC. M.I. acknowledges support from the Creative Initiative program, No. 2008-0060544, of the National Research Foundation of Korea (NRFK) funded by the Korean government (MSIP). M. D.J. acknowledges NSF grant AST-0618209 used for obtaining the 0.91 m telescope at WMO. SRON is financially supported by NWO, the Netherlands Organization for Scientific Research. B.C.K. is partially supported by the UC Center for Galaxy Evolution. C.S.K. acknowledges the support of NSF grant AST-1009756. D.C.L. acknowledges support from NSF grants AST-1009571 and AST-1210311, under which part of this research (photometric observations collected at MLO) was carried out. We thank Nhieu Duong, Harish Khandrika, Richard Mellinger, J. Chuck Horst, Steven Armen, and Eddie Garcia for assistance with the MLO observations. P.L. acknowledges support from Fondecyt grant #1120328. A.P. acknowledges support from an NSF graduate fellowship, a UCSB Dean's Fellowship, and a NASA Einstein Fellowship. J. S.S. acknowledges CNPq, National Council for Scientific and Technological Development (Brazil) for partial support and The Ohio State University for warm hospitality. T.T. has been supported by NSF grant AST-1412315. T.T. and B.C.K. acknowledge support from the Packard Foundation in the form of a Packard Research Fellowship to T.T.; also, T.T. thanks the American Academy in Rome and the Observatory of Monteporzio Catone for kind hospitality. The Dark Cosmology Centre is funded by the Danish National Research Foundation. M.V. gratefully acknowledges support from the Danish Council for Independent Research via grant no. DFF–4002-00275. J.-H.W. acknowledges support by the National Research Foundation of Korea (NRF) grant funded by the Korean government (No. 2010-0027910). E.D.B. is supported by Padua University through grants 60A02-5857/13, 60A02-5833/14, 60A02-4434/15, and CPDA133894. K.H. acknowledges support from STFC grant ST/M001296/1. S.A.K. thanks Dr. I. A. Rakhimov, the director of Svetloe Observatory, for his support and hospitality.

This research has made use of the NASA/IPAC Extragalactic Database (NED), which is operated by the Jet Propulsion Laboratory, California Institute of Technology, under contract with NASA.

APPENDIX
ON INTERPOLATION

Interpolating a light curve requires some assumed model, which may be more or less sophisticated. For example, linear interpolation is a very simple method. However, linear interpolation assumes no additional variability between sampled epochs, and this is known to be an incorrect description of AGN light curves on nightly timescales. The DRW allows for intrinsic variations between sampled epochs by modeling the data covariance, from which we can make a better guess as to what the continuum is doing between the observations and, moreover, assign a meaningful error bar to the prediction.

Figure 10 shows the linear interpolation model of a portion of the *R*-band continuum light curve of NGC 5548 (the *R* band was chosen because it has large gaps). By definition, the linearly interpolated model goes exactly through every data point. It has an "error snake" that matches the error bars of the data at a sampled epoch and can shrink between data points. This is because the model includes only measurement noise, so the error in the model is smallest somewhere in between the data points where it best averages the two measurements. Defining the fractional distance between the interpolated epoch t_j and the data points t_i and t_{i+1} as $x = (t_j - t_i)/(t_{i+1} - t_i)$ so $0 < x < 1$, the error snake for linear interpolation at t_j is given by $\sigma^2(t_j) = (1-x)^2\sigma(ti)^2 + x^2\sigma(t_{i+1})^2$, which is smallest at $x = 1/2$ for $\sigma(t_i) = \sigma(t_{i+1})$. Because it is required to go through the data points, there are regions of the model light curve (e.g., near day 6740) where the model rapidly "oscillates" in order to pass through nearby points. The principal problems with the linear interpolation model are therefore (1) that the model light curve has much more structure than it should when the light curve is well sampled, and (2) the error snake can decrease in width the farther it gets from the actual data points.

`JAVELIN` uses a covariance model to estimate the statistical properties of light curves. We have used the DRW model because it is simple and describes quasar variability on the timescales sampled by the data (Kelly et al. 2009; MacLeod et al. 2010; Zu et al. 2013). The middle panel of Figure 10 shows the DRW model for the same region of the NGC 5548 light curve. There are two important qualitative changes. First, unlike linear interpolation, the model no longer has to go through the data points. For example, in the region near day 6740, the DRW model is quite smooth because it has decided (statistically) that the three points with larger uncertainties should be viewed as measurement fluctuations rather than intrinsic variability. In contrast, there is the region near day 6758 where the error bars on the points forming a "triangle" are small enough that the model tracks the data points more or less like the linear interpolated model. The second difference is that the error snakes generally grow in the gaps between the data points. This is because `JAVELIN` is accounting for the intrinsic variability, as well as the measurement errors. The more distant an actual measurement, the greater the expected variance in the underlying

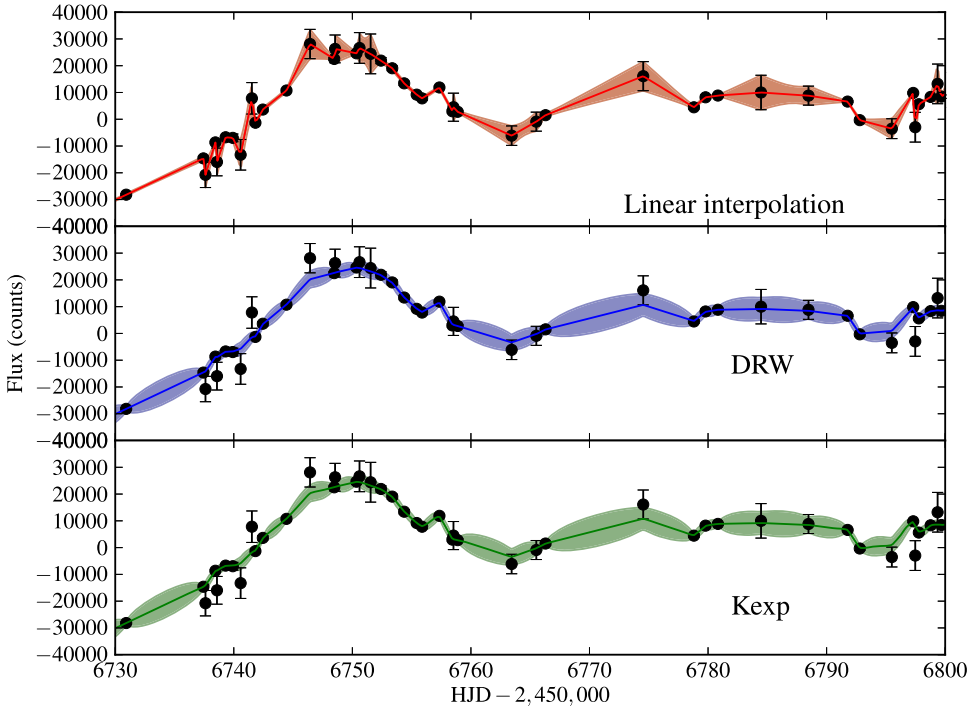

Figure 10. Data and models for the *R*-band continuum in NGC 5548. Top panel: linear interpolation model. Middle panel: DRW model. Bottom panel: "Kepler-exponential model," which is DRW with a drop in power on the shortest timescales ($\tau_{\rm cut} = 1$ day).

light curve. If the measurement errors are very large (e.g., the point near day 6785), then the error snake can be smaller than the measurement errors because the model predicts the expected range of the light curve better than it was actually measured.

There is evidence from high-cadence *Kepler* light curves that the DRW model overestimates the variability power on short (subweek) timescales (Edelson et al. 2014; Kasliwal et al. 2015). Although the DRW is therefore an incorrect model on short timescales, our data have very different properties from the *Kepler* light curves (1-day cadence instead of 30-minute cadence and ~0.5%–1.0% uncertainties instead of ~0.1%), and useful results can be found as long as the covariance model is a reasonable approximation of the true data covariance. An analogy exists here with optimal (Weiner) filters—quoting from *Numerical Recipes* (Press et al. 2002, chap. 13.3, p. 651), "In other words, even a fairly crudely determined optimal filter can give excellent results when applied to data." This is because errors in the covariance model only become significant when the differences are larger than the noise σ. For two structure-function amplitudes SF_1 and SF_2, the fractional changes in the models are of order $|\mathrm{SF}_1^2 - \mathrm{SF}_2^2|/\sigma^2$. Unless the light curve is of sufficiently high quality to measure the structure function on a given timescale, we will not have any noticeable effects from making even order unity errors in the structure function on those timescales. To go back to the optimal filtering analogy, we get 90% of the gains from being in the ballpark, and very little extra from being perfectly correct.

We can illustrate this by using the "Kepler-exponential" model from Zu et al. (2013), which includes a timescale $\tau_{\rm cut}$ below which the power spectrum is cut off. The Kepler-exponential model was designed to explore the *Kepler* results (that AGN light curves have suppressed power on short timescales) and is available as an option in `JAVELIN` (the `JAVELIN` algorithm can use any covariance model desired). The Kepler-exponential model of the *R*-band light curve is shown in Figure 10 with a power cutoff timescale $\tau_{\rm cut} = 1$ day.

Table 9
Comparison of DRW and Kepler-exponential Interpolations

Band	χ^2/dof (DRW)	χ^2/dof (Kexp)
u	0.37	0.34
B	0.29	0.29
g	0.33	0.31
V	0.65	0.73
r	0.40	0.40
R	0.41	0.41
i	0.23	0.22
I	0.28	0.26
z	0.27	0.26

As expected, it is very difficult to see any differences. The easiest one to spot is that the error snake grows a little faster as it moves away from a data point in the DRW model because it has some extra small-scale power (which actually makes the DRW model a more conservative choice). If we steadily increase $\tau_{\rm cut}$ above 1 day, the Kepler-exponential models start to fit the data poorly because they have too little short-timescale power.

We compared the DRW and Kepler-exponential models quantitatively by assessing how well they predict the data. We generated predicted values for each data point from the interpolation scheme described in Section 2.3 for each model and then calculated

$$\chi^2/\mathrm{dof} = \frac{1}{N-k}\sum_i^N \frac{(y_i - m_i)^2}{\sigma_i^2},$$

where N is the number of data points, k is the number of parameters, y are the data, m are the interpolated values, and σ are the uncertainties (on the data only—the uncertainty on the interpolation is necessarily consistent with the data). We use all data points when calculating the interpolation, and so we

emphasize that this definition has nothing to do with the probability of the model: linear interpolation would force this value of $\chi^2/\mathrm{dof} = 0$, even though it is certainly not correct. Rather, this definition gives an estimate of the consistency of the data with the model. For these fits, we again fixed $\tau_{\rm cut}$ to 1 day.

Table 9 summarizes these results. The two models produce interpolations that are virtually indistinguishable (i.e., nearly equal χ^2/dof). Increasing $\tau_{\rm cut}$ to 10 days increases χ^2/dof by a small amount (up to 0.06), and as $\tau_{\rm cut}$ approaches 0 days, we recover the DRW. This means that there is no quantitative advantage to using a random process with suppressed short-timescale power—our data are not good enough to see this effect.

REFERENCES

Abazajian, K. N., Adelman-McCarthy, J. K., Agüeros, M. A., et al. 2009, ApJS, 182, 543
Abramowicz, M. A., Czerny, B., Lasota, J. P., & Szuszkiewicz, E. 1988, ApJ, 332, 646
Alard, C., & Lupton, R. H. 1998, ApJ, 503, 325
Arévalo, P., Uttley, P., Lira, P., et al. 2009, MNRAS, 397, 2004
Barth, A. J., Bennert, V. N., Canalizo, G., et al. 2015, ApJS, 217, 26
Bentz, M. C., Denney, K. D., Grier, C. J., et al. 2013, ApJ, 767, 149
Bentz, M. C., Horne, K., Barth, A. J., et al. 2010a, ApJL, 720, L46
Bentz, M. C., & Katz, S. 2015, PASP, 127, 67
Bentz, M. C., Walsh, J. L., Barth, A. J., et al. 2009, ApJ, 705, 199
Bentz, M. C., Walsh, J. L., Barth, A. J., et al. 2010b, ApJ, 716, 993
Blandford, R. D., & McKee, C. F. 1982, ApJ, 255, 419
Breedt, E., Arévalo, P., McHardy, I. M., et al. 2009, MNRAS, 394, 427
Breedt, E., McHardy, I. M., Arévalo, P., et al. 2010, MNRAS, 403, 605
Brosch, N., Polishook, D., Shporer, A., et al. 2008, Ap&SS, 314, 163
Bruzual, G., & Charlot, S. 2003, MNRAS, 344, 1000
Burbidge, E. M. 1967, ARA&A, 5, 399
Cackett, E. M., Gültekin, K., Bentz, M. C., et al. 2015, ApJ, 810, 86
Cackett, E. M., Horne, K., & Winkler, H. 2007, MNRAS, 380, 669
Cardelli, J. A., Clayton, G. C., & Mathis, J. S. 1989, ApJ, 345, 245
Chakrabarti, S., & Titarchuk, L. G. 1995, ApJ, 455, 623
Chelouche, D. 2013, ApJ, 772, 9
Chelouche, D., & Zucker, S. 2013, ApJ, 769, 124
Chiang, J., & Murray, N. 1996, ApJ, 466, 704
Cid Fernandes, R., Gu, Q., Melnick, J., et al. 2004, MNRAS, 355, 273
Clavel, J., Reichert, G. A., Alloin, D., et al. 1991, ApJ, 366, 64
Collier, S. J., Horne, K., Kaspi, S., et al. 1998, ApJ, 500, 162
Collin, S., Boisson, C., Mouchet, M., et al. 2002, A&A, 388, 771
Collin-Souffrin, S. 1987, A&A, 179, 60
De Rosa, G., Peterson, B. M., Ely, J., et al. 2015, ApJ, 806, 128 (Paper I)
Denney, K. D. 2012, ApJ, 759, 44
Denney, K. D., Peterson, B. M., Dietrich, M., Vestergaard, M., & Bentz, M. C. 2009, ApJ, 692, 246
Denney, K. D., Peterson, B. M., Pogge, R. W., et al. 2010, ApJ, 721, 715
Dietrich, M., Hamann, F., Shields, J. C., et al. 2002, ApJ, 581, 912
Edelson, R., Gelbord, J. M., Horne, K., et al. 2015, ApJ, 806, 129 (Paper II)
Edelson, R., Vaughan, S., Malkan, M., et al. 2014, ApJ, 795, 2
Eracleous, M., Lewis, K. T., & Flohic, H. M. L. G. 2009, NewAR, 53, 133
Filippenko, A. V., Li, W. D., Treffers, R. R., & Modjaz, M. 2001, in ASP Conf. Ser. 246, Small Telescope Astronomy on Global Scales, ed. B. Paczynski, W.-P. Chen, & C. Lemme (San Francisco, CA: ASP), 121
Fukugita, M., Ichikawa, T., Gunn, J. E., et al. 1996, AJ, 111, 1748
Gehrels, N., Chincarini, G., Giommi, P., et al. 2004, ApJ, 611, 1005
Goad, M. R., Korista, K. T., & Ruff, A. J. 2012, MNRAS, 426, 3086
Green, J. C., Froning, C. S., Osterman, S., et al. 2012, ApJ, 744, 60
Grier, C. J., Martini, P., Watson, L. C., et al. 2013a, ApJ, 773, 90
Grier, C. J., Peterson, B. M., Horne, K., et al. 2013b, ApJ, 764, 47
Haardt, F., & Maraschi, L. 1991, ApJL, 380, L51
Hartman, J. D., Bakos, G., Stanek, K. Z., & Noyes, R. W. 2004, AJ, 128, 1761
Higginbottom, N., Proga, D., Knigge, C., et al. 2014, ApJ, 789, 19
Hill, J. M., Green, R. F., Ashby, D. S., et al. 2010, Proc. SPIE, 7733, 0
Horne, K., Peterson, B. M., Collier, S. J., & Netzer, H. 2004, PASP, 116, 465
Horne, K., Welsh, W. F., & Peterson, B. M. 1991, ApJL, 367, L5
Jiang, Y.-F., Stone, J. M., & Davis, S. W. 2014, ApJ, 796, 106
Kasliwal, V. P., Vogeley, M. S., & Richards, G. T. 2015, MNRAS, 451, 4328
Kaspi, S., Smith, P. S., Netzer, H., et al. 2000, ApJ, 533, 631
Kelly, B. C., Bechtold, J., & Siemiginowska, A. 2009, ApJ, 698, 895
Kishimoto, M., Antonucci, R., Boisson, C., & Blaes, O. 2004, MNRAS, 354, 1065
Komatsu, E., Smith, K. M., Dunkley, J., et al. 2011, ApJS, 192, 18
Koratkar, A., & Blaes, O. 1999, PASP, 111, 1
Korista, K. T., & Goad, M. R. 2001, ApJ, 553, 695
Korista, K. T., & Goad, M. R. 2004, ApJ, 606, 749
Krolik, J. H., Horne, K., Kallman, T. R., et al. 1991, ApJ, 371, 541
Laor, A., Jannuzi, B. T., Green, R. F., & Boroson, T. A. 1997, ApJ, 489, 656
Li, Y.-R., Wang, J.-M., Ho, L. C., Du, P., & Bai, J.-M. 2013, ApJ, 779, 110
Lira, P., Arévalo, P., Uttley, P., McHardy, I. M. M., & Videla, L. 2015, MNRAS, 454, 368
MacLeod, C. L., Ivezić, Ž, Kochanek, C. S., et al. 2010, ApJ, 721, 1014
Maoz, D., Markowitz, A., Edelson, R., & Nandra, K. 2002, AJ, 124, 1988
Marshall, K., Ryle, W. T., & Miller, H. R. 2008, ApJ, 677, 880
McHardy, I. M., Cameron, D. T., Dwelly, T., et al. 2014, MNRAS, 444, 1469
Mehdipour, M., Kaastra, J. S., Kriss, G. A., et al. 2015, A&A, 575, A22
Morgan, C. W., Kochanek, C. S., Morgan, N. D., & Falco, E. E. 2010, ApJ, 712, 1129
Mosquera, A. M., Kochanek, C. S., Chen, B., et al. 2013, ApJ, 769, 53
Narayan, R., & Yi, I. 1995, ApJ, 452, 710
Netzer, H. 2013, The Physics and Evolution of Active Galactic Nuclei (Cambridge: Cambridge Univ. Press)
Novikov, I. D., & Thorne, K. S. 1973, in Black Holes (Les Astres Occlus), ed. C. Dewitt, & B. S. Dewitt (Paris: Gordon and Breach), 343
Onken, C. A., Ferrarese, L., Merritt, D., et al. 2004, ApJ, 615, 645
Pancoast, A., Brewer, B. J., Treu, T., et al. 2014, MNRAS, 445, 3073
Park, D., Kelly, B. C., Woo, J.-H., & Treu, T. 2012a, ApJS, 203, 6
Park, D., Woo, J.-H., Treu, T., et al. 2012b, ApJ, 747, 30
Pei, L., Barth, A. J., Aldering, G. S., et al. 2014, ApJ, 795, 38
Peterson, B. M. 1993, PASP, 105, 247
Peterson, B. M. 2001, in Advanced Lectures on the Starburst-AGN, ed. I. Aretxaga, D. Kunth, & R. Mújica (Singapore: World Scientific), 3
Peterson, B. M. 2014, SSRv, 183, 253
Peterson, B. M., Balonek, T. J., Barker, E. S., et al. 1991, ApJ, 368, 119
Peterson, B. M., Ferrarese, L., Gilbert, K. M., et al. 2004, ApJ, 613, 682
Pogge, R. W., Atwood, B., Brewer, D. F., et al. 2010, Proc. SPIE, 7735, 0
Poindexter, S., Morgan, N., & Kochanek, C. S. 2008, ApJ, 673, 34
Poole, T. S., Breeveld, A. A., Page, M. J., et al. 2008, MNRAS, 383, 627
Press, W. H., Teukolsky, S. A., Vetterling, W. T., & Flannery, B. P. 2002, Numerical Recipes in C++: The Art of Scientific Computing (Cambridge: Cambridge Univ. Press)
Proga, D., & Kallman, T. R. 2004, ApJ, 616, 688
Proga, D., & Kurosawa, R. 2010, in ASP Conf. Ser. 427, Accretion and Ejection in AGN: A Global View, ed. L. Maraschi et al. (San Francisco, CA: ASP), 41
Rodríguez-Pascual, P. M., Alloin, D., Clavel, J., et al. 1997, ApJS, 110, 9
Sądowski, A., Narayan, R., McKinney, J. C., & Tchekhovskoy, A. 2014, MNRAS, 439, 503
Sakata, Y., Minezaki, T., Yoshii, Y., et al. 2010, ApJ, 711, 461
Schlafly, E. F., & Finkbeiner, D. P. 2011, ApJ, 737, 103
Schlegel, D. J., Finkbeiner, D. P., & Davis, M. 1998, ApJ, 500, 525
Sergeev, S. G., Doroshenko, V. T., Golubinskiy, Y. V., Merkulova, N. I., & Sergeeva, E. A. 2005, ApJ, 622, 129
Shakura, N. I., & Sunyaev, R. A. 1973, A&A, 24, 337
Shappee, B. J., Prieto, J. L., Grupe, D., et al. 2014, ApJ, 788, 48
Shields, G. A. 1978, Natur, 272, 706
Skielboe, A., Pancoast, A., Treu, T., et al. 2015, MNRAS, 454, 144
Steele, I. A., Smith, R. J., Rees, P. C., et al. 2004, Proc. SPIE, 5489, 679
Sun, W.-H., & Malkan, M. A. 1989, ApJ, 346, 68
Telfer, R. C., Zheng, W., Kriss, G. A., & Davidsen, A. F. 2002, ApJ, 565, 773
Troyer, J., Starkey, D., Cackett, E. M., et al. 2016, MNRAS, 456, 4040
Uttley, P., Edelson, R., McHardy, I. M., Peterson, B. M., & Markowitz, A. 2003, ApJL, 584, L53
Vaughan, S., Edelson, R., Warwick, R. S., & Uttley, P. 2003, MNRAS, 345, 1271
Vestergaard, M., & Peterson, B. M. 2005, ApJ, 625, 688
Vestergaard, M., & Wilkes, B. J. 2001, ApJS, 134, 1
Wanders, I., Peterson, B. M., Alloin, D., et al. 1997, ApJS, 113, 69
Welsh, W. F. 1999, PASP, 111, 1347
Woo, J.-H., Schulze, A., Park, D., et al. 2013, ApJ, 772, 49
Woo, J.-H., Treu, T., Barth, A. J., et al. 2010, ApJ, 716, 269
Woo, J.-H., Yoon, Y., Park, S., Park, D., & Kim, S. C. 2015, ApJ, 801, 38
Zu, Y., Kochanek, C. S., Kozłowski, S., & Udalski, A. 2013, ApJ, 765, 106
Zu, Y., Kochanek, C. S., & Peterson, B. M. 2011, ApJ, 735, 80